University of Illinois at Urbana-Champaign

ACRC

Air Conditioning and Refrigeration Center   A National Science Foundation/University Cooperative Research Center

Investigation of the Scuffing Mechanism for Gray Cast Iron Undergone Tribological Testing Using Macro-, Micro-, and Nano- Analytical Techniques

A. Y. Suh, A. A. Polycarpou, and T. F. Conry

ACRC TR-212   March 2003

For additional information:

Air Conditioning and Refrigeration Center
University of Illinois
Mechanical & Industrial Engineering Dept.
1206 West Green Street
Urbana, IL 61801

(217) 333-3115

Table of Contents

List of Figures

List of Tables

Chapter 1. Introduction

This is a study carried out to understand better the wear properties of gray cast iron leading to sudden, catastrophic damage of surfaces known as scuffing. Factors influencing scuffing include pressure, velocity, temperature, lubrication, surface topography, materials and metallurgical aspects, and film coatings of surfaces in contact (Pergande, 2001). In the context of contacting surfaces found in air conditioning compressors, understanding of the wear-scuffing mechanisms was conducted by investigating various changes found on the surface mainly at sub-micron level. The test includes gray cast iron samples as both the pin and disk in a pin on disk geometry. The cast iron samples were be tested on the High Pressure Tribometer (HPT) under prescribed conditions to simulate scuffing as well as intermediate wear stages prior to scuffing. Because scuffing is a phenomenon that brings drastic changes to the surface on many levels, several engineering tools and scientific techniques were adopted to best capture and characterize these changes. This report is divided into five individual chapters, each dealing with unique investigative method in an effort to substantiate and quantify changes occurring at the topmost surface as well as the sub-surface layer. The chapters are categorized as the following;

- **Chapter 2** – Experimental HPT scuffing tests on gray cast iron disk samples and wear track analysis by Dektak 1-D surface profilometer
- **Chapter 3** – 1-D surface roughness characterization and comparative study of surface parameters on iron disks and pins
- **Chapter 4** –Micro-structural analysis by the Scanning Electron Microscope (SEM)
- **Chapter 5** –Nano-scale surface and sub-surface chemical analysis by the Auger Electron Spectroscopy (AES)
- **Chapter 6** –Material property analysis by macro-, micro-, and nano- hardness tests

In the present study, the step-loading test procedure was used for the scuffing experiments. A 20 lb load step and a step duration of 15 seconds was used. The 15-second step duration was chosen since, under starved lubrication conditions, a steady state temperature was reached after approximately 10 seconds (Yoon, 1999). These parameters were chosen based on Cavatorta's study (2000), and after conducting many trials to obtain repeatable scuffing results. In this study, scuffing was determined by sharp transitions of the contact resistance (indicating the destruction of surface films), and friction coefficient transition. The process of stepwise loading eventually led to scuffing failure, which caused sharp transitions of the contact resistance, and friction coefficient. At this stage, the load was quickly released and the test stopped. The time taken to scuff the sample was noted as T_{scuff} and three other tests were run with the same parameters, but the tests were stopped prior to scuffing at ¼ x T_{scuff}, ½ x T_{scuff} and ¾ x T_{scuff}.

Chapter 2. High-Pressure-Tribometer Scuffing Tests

2.1 Test Protocol Summary

1.) Five cast iron samples were selected, making sure they have little surface damage from scratches.

2.) Sample preparation; The 5 samples were immersed in pools of Acetone, and ultrasonically cleaned for 10 minutes. They were then rinsed in alcohol and dried using a heat source. The samples were then placed in sealed containers to prevent contamination. Note that the specimen were wrapped in aluminum foil and were not in direct contact with the plastic container for it will be subject to carbon contamination.

3.) Initial surface roughness; the samples were marked and their surface roughness measured both on pins and disks.

4.) HPT testing; the five samples were to be tested under starved lubrications as follows:

If T_{scuff} = time to scuff,

- Sample 1; Virgin sample, no Tribological testing.
- Sample 2; Sample was tested for a time corresponding to ¼ x T_{scuff}
- Sample 3; Sample was tested for a time corresponding to ½ x T_{scuff}
- Sample 4; Sample was tested for a time corresponding to ¾ x T_{scuff}.
- Sample 5; Sample was tested until it scuffed, time taken to scuff (T_{scuff}) noted.

5.) The operating conditions for the HPT were as follows;

- Rotation Speed; 1030 RPM (2.4m/s)
- Step Load; 20 lbs with initial load of 20lb
- Disk Temperature; 121°C
- Loading Interval; 15 seconds
- 0.2 Torr Vacuum

6.) After the testing, the samples were then ultrasonically cleaned as mentioned above, and 1-D profilometer scans to measure surface roughness are run similar to those on the virgin sample.

7.) The roughness data were analyzed using a computer program (MatLab) and Greenwood and Williamson (1966) micro-contact parameters were extracted.

8.) The samples were then cut into smaller sizes using a low speed diamond saw, and prepared for chemical analysis (prior to analysis they were ultrasonically cleaned again).

2.2 HPT Experimental Results and Analysis

In this section the data output from the HPT was analyzed. The data were plotted in the following temporal order ¼ x T_{scuff}, ½ x T_{scuff}, ¾ x T_{scuff} and finally T_{scuff} (scuffing time based on the sudden increase in contact resistance and friction from the HPT). The actual experimentation time that led to scuffing, as denoted T_{scuff}, was 7 minutes (it should be noted that prior experiments were done under similar conditions with similar samples, to confirm that the time T_{scuff} for scuffing is in fact correct in this case. This was important because all other following experiments are to be based on this time). A possible problem with the short duration of the tests was the fact that it might be too

vigorous. However, if the loading time was increased or rotation speed decreased, the sample did not scuff within the time allowed by the refrigerant supply (the volume of refrigerant is constant thus the sample should scuff before the tests runs out of refrigerant). The experiments that were stopped prior to scuffing, were done so manually. Figures 1-4 show the HPT experiments for samples 2 to 5, respectively. Note that load is in lbf whereas friction coefficient and contact resistance are unitless.
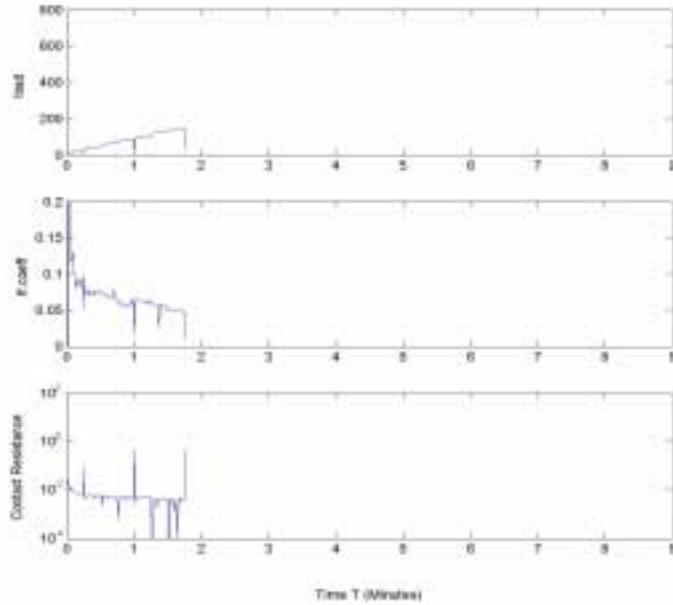
Figure 1. Sample 2 - ¼ x T_{scuff}
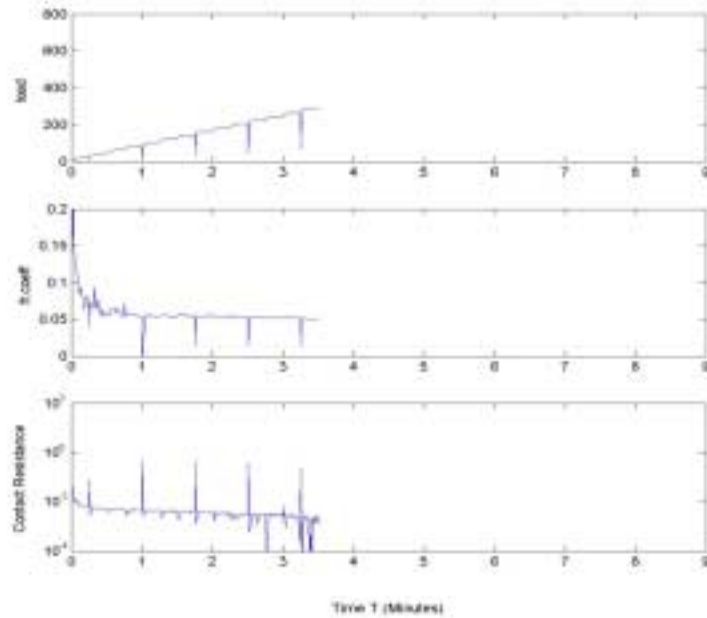
Figure 2. Sample 3 - ½ x T_{scuff}
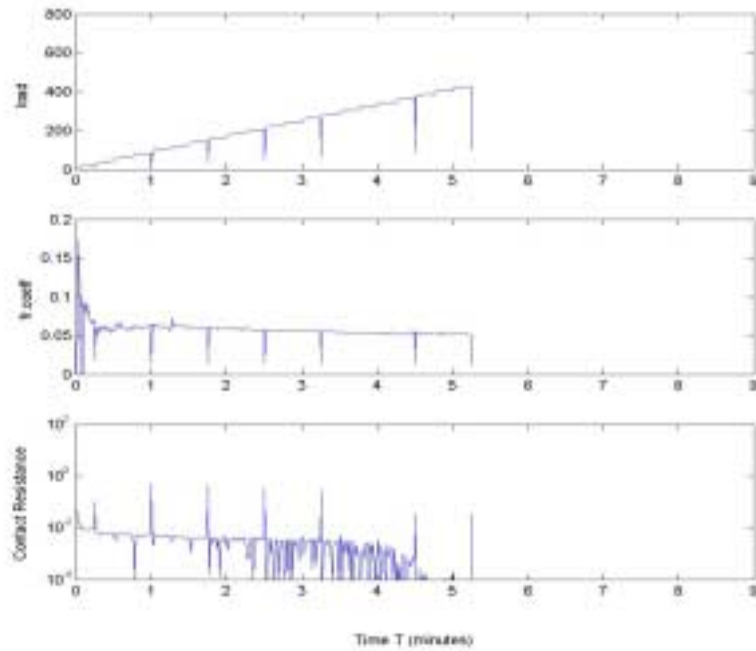
Figure 3. Sample 4 – ¾ x T_{scuff}
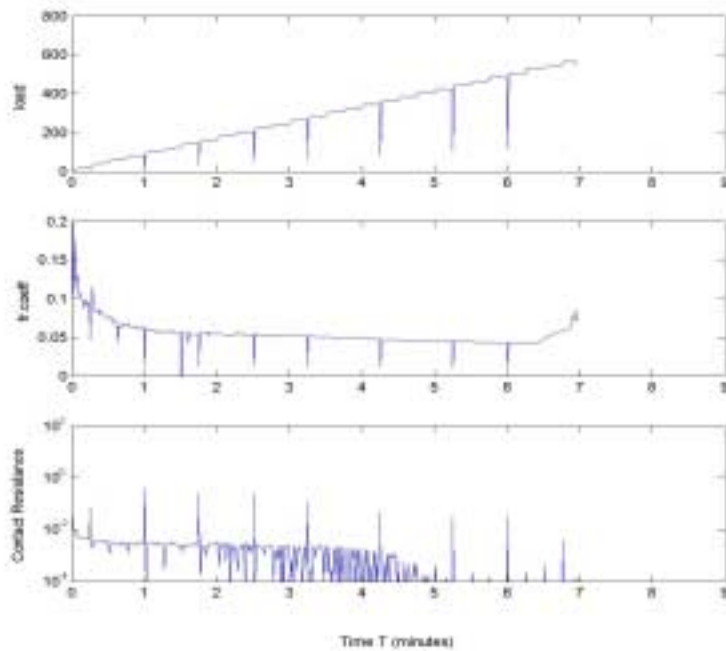
Figure 4. Sample 5 - T_{scuff}

2.2.1 Load versus Time

The load applied to the pin on disk system was applied in steps as described earlier. These figures show an increase in load every 15 seconds until the experiment is stopped. The vertical lines dropping down in the plot are electric noise and therefore should be ignored.

2.2.2 Friction Coefficient versus Time

The friction coefficient is a representation of the physical resistance to motion experienced by the disk on pin. Initially the friction coefficient was higher and erratic due to taller asperities. As these peaks were smoothened out, the friction coefficient dropped and stabilized at an almost constant value (i.e. running in). In the case of the scuffed experiment, the friction coefficient increased due to the fact that the adhesion force between the disk and pin increased as the asperities were smoothened out. This increase in adhesion force caused an increase in the friction coefficient. It was suggested that in this case the scuffed sample failed due to adhesive failure.

2.2.3 Contact Resistance versus Time

The contact resistance represents the percent of asperity contact in the case of both asperity and lubricant presence within the interface. If the samples are fully separated, the contact resistance is infinite. On the other hand, if the asperities have significant contact (metal contact), the contact resistance should be zero. If the contact resistance is in the range 10^{-2} to 10^2 ohms, the lubrication regimes that exist are boundary and mixed. For instance, a contact resistance of 10^{-2} is translated into a lot of contacting asperities, whereas that of 10^2 means a lot less. For the data shown previously the contact resistance was not as expected, probably due to a fault in the wire connection. This data was therefore ignored in this analysis.

2.3 Micrograph Analysis

In this section, the virgin state to the worn state of the samples were studied at the micro scale. Figure 5 shows the gross images of iron disk samples from virgin to scuffed states.
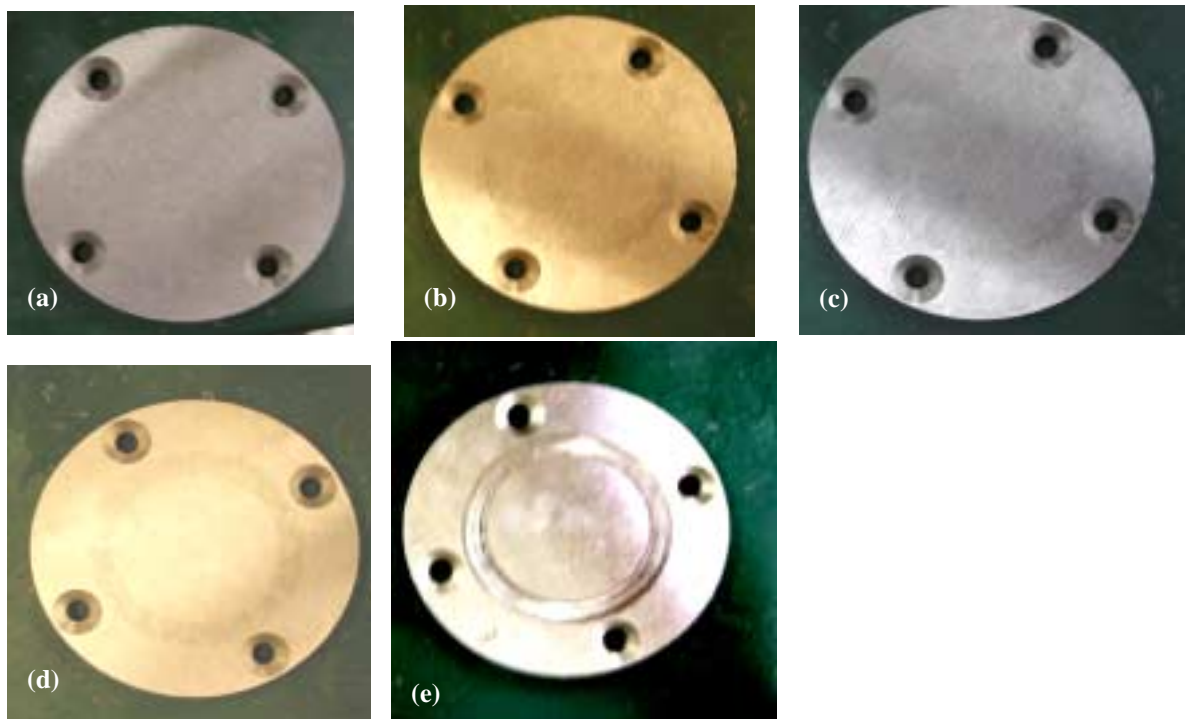
Figure 5. Cast iron samples (a) Virgin, (b) ¼ T_{scuff}, (c) ½ T_{scuff}, (d) ¾ T_{scuff}, and (e) T_{scuff}

Notice from Figure 5 that although faint wear tracks existed in all of the worn samples, wear track was the most markedly visible only on Sample 5 (i.e. T_{scuff} stage), with an existence of significant material removal and transfer.

2.4 Radial Direction - Long Scan Data

The 1-D Dektak scans made in the radial direction were long scans made across the wear track as to see the cross-sectional damage done by the pin on the gray cast iron disk. These scans were composed of 8000 data points and were 10 mm long, covering the whole wear track (7mm). Obtaining these scans allowed "wear volume" calculation, or how much material was removed due to wear damage, based on geometric observation. The long scans covered both the virgin and worn parts, therefore were used to comparatively study the deformation of the surface as it was subject to wear. In the following section, the wear scans moving from the virgin to their respective worn states are discussed briefly.

2.4.1 Radial long scan on virgin sample

This scan was carried out on a virgin surface, which had undergone no testing. As can be seen from Figure 6 the surface was fairly rough composed of both peaks and valleys. The first changes that occur from this surface can be viewed on sample 2 surface scan.

OD (Outer Diameter)   *ID (inner Diameter)*
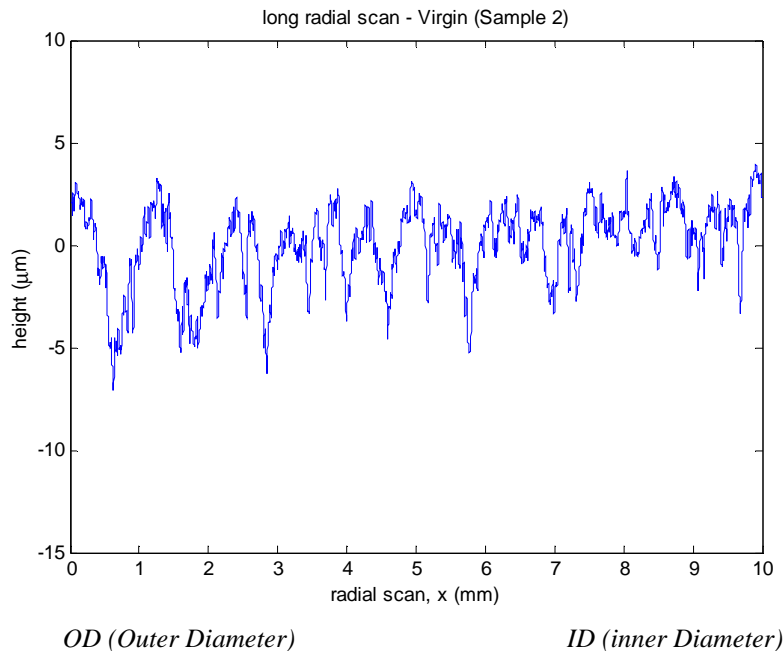
Figure 6. Radial long scan on virgin surface

2.4.2 Radial long scan on ¼ x T_{scuff} sample

As shown in Figure 7, no significant polishing of asperities was observed at ¼ x T_{scuff} although there seemed to be some material removal at the inner diameter region (ID). Unlike in the case of Al390-T6 (Patel, 2001) where a primary wear track already existed at this point around the mid-section, there was no seemingly evident wear track at this stage. This may be due to the fact that cast iron is generally harder than aluminum alloy, hence no well-defined wear track. The surface was now subject to more wear at ½ x T_{scuff} to reveal the change in topography.

long radial scan covering the wear track - Sample 2 (1/4 x T$_{scuff}$)

OD (Outer Diameter)   ID (inner Diameter)
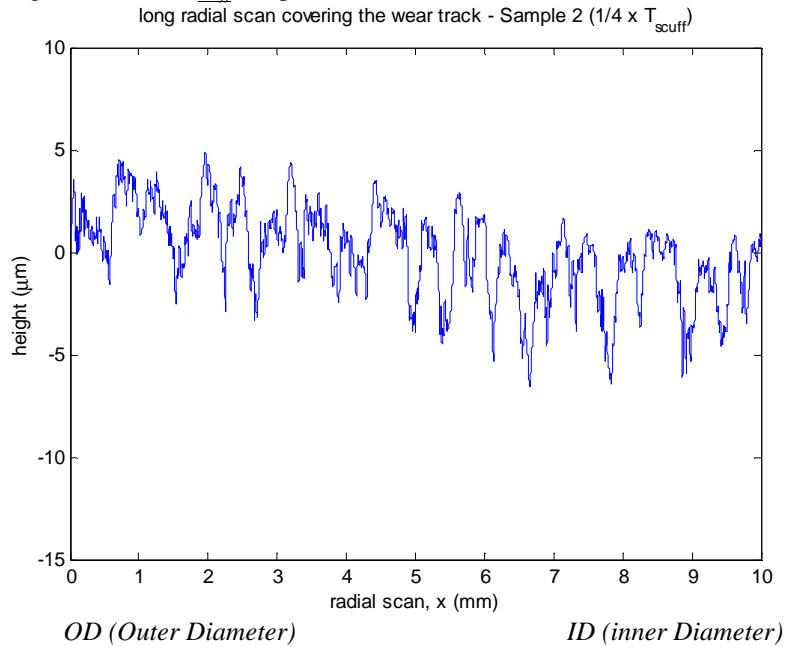
Figure 7. Radial long scan on ¼ x T_{scuff} surface (Sample 2 after HPT test)

The scan displayed in Figure 8 shows that the asperities in the previous scan were somewhat more polished with a bowed region in the middle to indicate material removal due to progressive wear. The wear track position could be established at 1-2 mm and 8-9 mm, although material displacement was still difficult to notice. The same trend as before was observed here; there still were no apparent primary wear scars. This corresponds to the visual observation previously made (refer back to Figure 5(c)). From the removal of material, the surface was evidently undergoing more drastic changes as it neared scuffing.

long radial scan covering the wear track - Sample 3 (1/2 x T$_{scuff}$)

OD (Outer Diameter)   ID (inner Diameter)
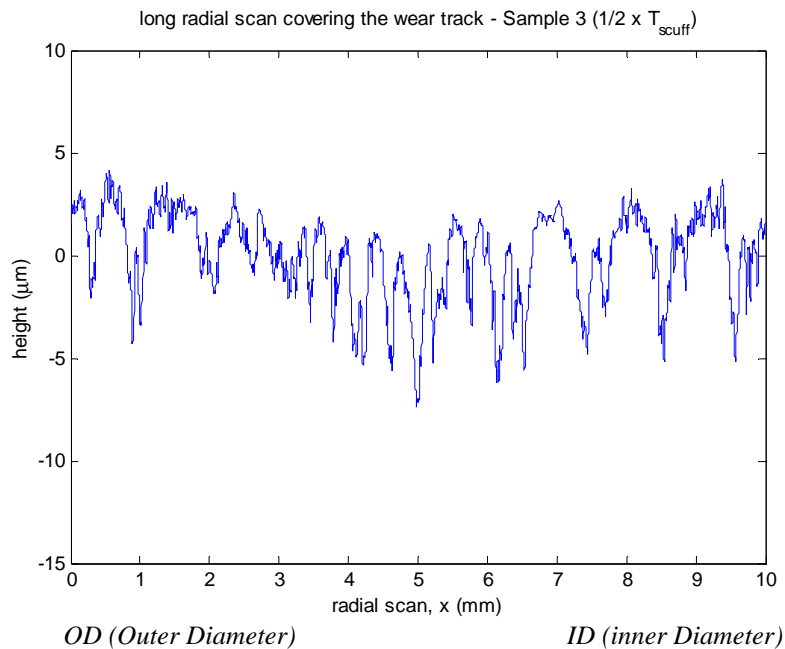
Figure 8. Radial long scan on ½ x T_{scuff} surface (Sample 3 after HPT test)

<u>2.4.4 Radial long scan on ¾ x T_{scuff} sample</u>

As the surface was progressively worn towards scuffing, rather than more smoothening of the asperities, cyclical material transfer seemed to occur as depicted in Figure 9. There was however, general smoothening of the asperities in the middle section of wear track. However, well-defined wear track boundaries were still absent even at this stage.

long radial scan covering the wear track - Sample 4 (3/4 x T_{scuff})

OD (Outer Diameter)   *ID (inner Diameter)*
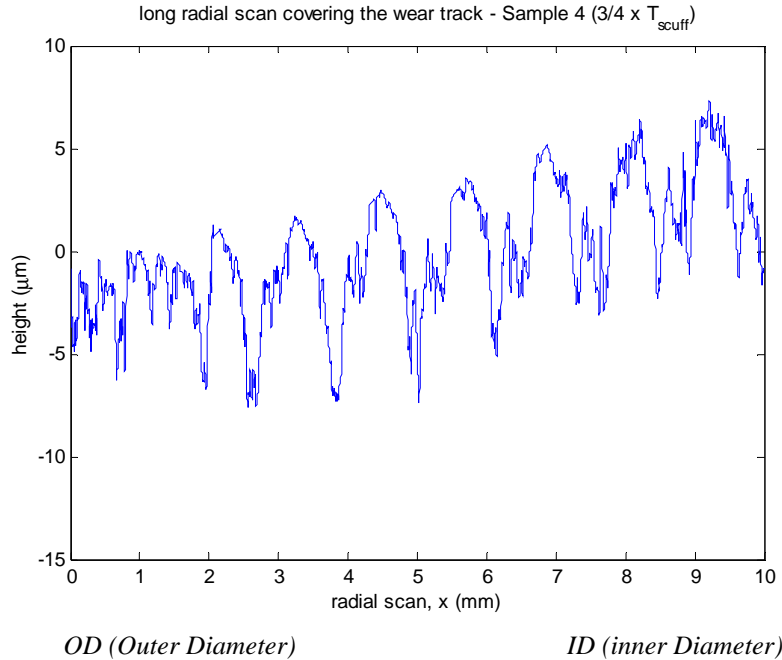
Figure 9. Radial long scan on ¾ x T_{scuff} surface (Sample 4 after HPT test)

<u>2.4.5 Radial long scan on T_{scuff} sample</u>

Material transfer occurs when a surface is scuffed, and it is displayed by Figure 10. There appeared to be non-uniformly distributed removal of material throughout the length of horizontal scan axis. Unlike in the case of Al390-T6 alloys where a mountain of material from the surrounding areas was observed at scuffing (Patel, 2001), this did not happen in scuffed cast iron. One interesting observation made from this figure was the lack of reduction in the surface height variation at the onset of scuffing, though the asperities were expected to be polished considerably at this point. From the wear scan analysis at scuffing, it was concluded that the wear mechanism of gray cast iron was perhaps markedly different from that of aluminum alloy.

long radial scan covering the wear track - Sample 5 (T_{scuff})
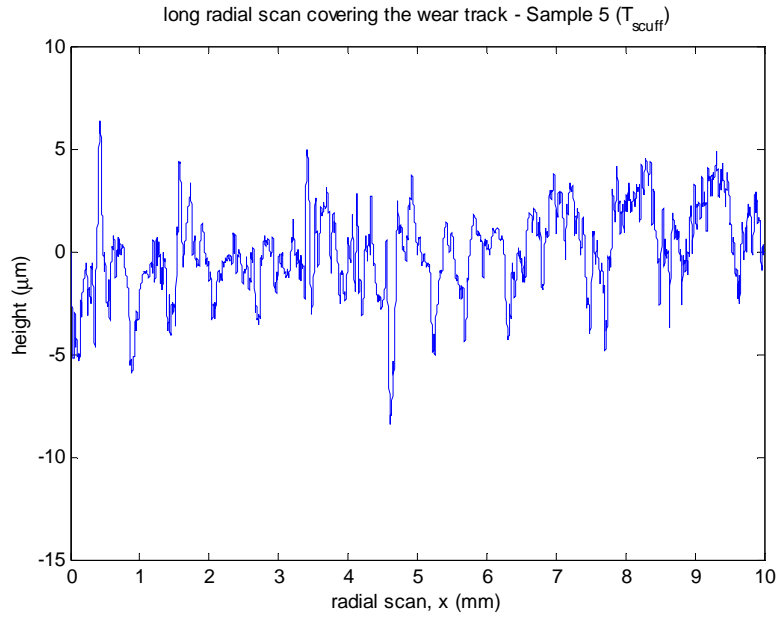
OD (Outer Diameter)   *ID (inner Diameter)*

Figure 10. Radial long scan on T_{scuff} surface (Sample 5 after HPT test)

Chapter 3. Surface Roughness Characterization
by the GW Statistical Roughness Model

3.1 Introduction of the Greenwood-Williamson statistical roughness model

This section of the report deals with analysis of statistical surface roughness parameters. The five cast iron disks were ultrasonically cleaned following the protocol that was described earlier, and 1-D Dektak profilometer scans were made on the surfaces. Three profilometer scans each 2 mm long were taken, consisting of 8000 data points. These scans are termed as short scans for the rest of the study (all scans were perpendicular to the machining marks). The short scans were taken in the worn section of the disk thus were primarily for statistical analysis.

The data obtained from the contact profilometer were analyzed based on the Greenwood-Williamson (GW) (1966) model to extract the necessary parameters. The GW model of contacting rough surfaces assumes that when two nominally flat surfaces touch, contact occurs on the local high spots or asperity summits. Deformation occurs in the contacting region and could either be elastic, plastic or elastic-plastic depending on the contact pressure and material properties of the surfaces. All the summits are presumed to be spherical and have the same radius R, but the summit heights 'z' are variable with a standard deviation σ. The asperities are assumed to be uniformly distributed over the rough surface with a density of asperities or denoted η. The GW model also suggested, based on experimental results, that for many engineering surfaces the distribution of asperity heights tends to be Gaussian. Modifications to this theory were made by McCool (1986), in which the foundation of the rough parameters was based on the existence of an isotropic surface where $z(x)$ is the height distribution of the surface profile. From this, three spectral moments of the surface can be defined;

$$ m_0 = AVG[z^2] \qquad m_2 = AVG[(dz/dx)^2] \qquad m_4 = AVG[(d^2 z/dx^2)^2] $$

From these spectral moments the three surface parameters are obtained as follows McCool (1986);

$$ \sigma = (m_0)^{1/2} \qquad R = 0.375(\pi/m_4)^{1/2} \qquad \eta = m_4 / \left[6\pi(3m_2)^{1/2}\right] $$

The R_a or "Center-Line-Average" and the R_q (i.e., σ) or "Root-Mean-Square" are the most widely used roughness parameters. For a surface where the height of the surface measured above a mean level, x is the coordinate on the surface, and L the measured length, the formula for obtaining R_a and R_q are given below.

$$ R_a = \frac{1}{L}\int_0^L |z| dx \qquad \text{and} \qquad R_q = \sqrt{\frac{1}{L}\int_0^L z^2 dx} $$

The third parameter used in this study is skewness, which is a descriptor of the degree of asymmetry (it is also the third moment). A negative skewness value indicates the existence of more valleys (area) than peaks and vice versa for a positive skewness. Kurtosis is the fourth moment of the normalized distribution, and it has a value of 3 for a Gaussian distribution. Distributions with peaks sharper than Gaussian have values of kurtosis greater than this, and vice versa. The equations for these parameters are given below:

$$ Sk = \frac{1}{\sigma^3}\int_{-\infty}^{+\infty} z^3 \phi(z) dz \qquad Ku = \frac{1}{\sigma^4}\int_{-\infty}^{+\infty} z^4 \phi(z) dz $$

where *Sk* is skewness and *Ku* is kurtosis. The above equations are used to derive the parameters used for the analysis of data obtained from the contact profilometer.

3.2 Disk Surface Roughness Analysis

Below is the list of wear subject to each sample:

- Sample 1 - Virgin sample, no wear test.
- Sample 2 - Sample was worn in for a time corresponding to ¼ x T_{scuff}
- Sample 3 - Sample was worn in for a time corresponding to ½ x T_{scuff}
- Sample 4 - Sample was worn in for a time corresponding to ¾ x T_{scuff}
- Sample 5 - Sample was run till it scuffed, time taken to scuff (T_{scuff}) noted.

The gray cast iron disk data obtained from the profilometer were analyzed using Matlab to determine the statistical parameters aforementioned. Table 1 summarizes the seven roughness parameters characterized for the iron disks each before and after the HPT tribological testing. The analyzed roughness parameters were plotted for the disk at each worn stage, and were discussed in this section.

Table 1. Statistical roughness parameters for cast iron samples before and after HPT testing

		Sample 1 (Virgin)	Sample 2 (¼ x Tscuff)	Sample 3 (½ x Tscuff)	Sample 4 (¾ x Tscuff)	Sample 5 (Tscuff)
R_a (µm)	Virgin	2.25	1.89	1.76	2.40	2.86
	Worn		1.32	1.43	1.20	1.66
R_q (µm)	Virgin	2.82	2.32	2.22	3.00	3.52
	Worn		1.57	1.78	1.52	2.06
R (µm)	Virgin	2.22	2.63	2.35	2.33	2.43
	Worn		3.05	3.30	3.00	3.46
η (µm^{-2})	Virgin	3.07 x 10^{-2}	3.65 x 10^{-2}	3.30 x 10^{-2}	3.00 x 10^{-2}	3.26 x 10^{-2}
	Worn		3.48 x 10^{-2}	3.33 x 10^{-2}	3.54 x 10^{-2}	2.20 x 10^{-2}
β	Virgin	0.19	0.23	0.17	0.21	0.28
	Worn		0.17	0.20	0.16	0.15
Sk	Virgin	-0.13	-0.57	-0.45	-0.76	-0.71
	Worn		-0.62	-0.61	-0.58	-0.29
Ku	Virgin	3.61	2.92	3.08	3.46	3.07
	Worn		2.43	2.88	3.22	3.10

3.2.1 Center Line Average (R_a) Trends on Cast Iron Disks

Figure 11 is a plot that summarizes all the average R_a values for the 5 disks in the study the standard deviation of al the virgin scans in the circumferential direction is 0.0714 µm. The error bar used in the figures is for ± one standard deviation. The data plotted are an average of all the 3 points in a specific direction on a given disk as

explained earlier. The general trend in this graph was that as the surface moved from virgin to worn stage, the R_a reduced; the peak asperities were worn out and the surface got polished. Like the aluminum surface (Patel, 2001) the cast iron was polished significantly by ¾ x T_{scuff}. The surfaces became smoother in their worn stages as compared to their virgin states. Similarly, the results from the R_q trends were investigated next.
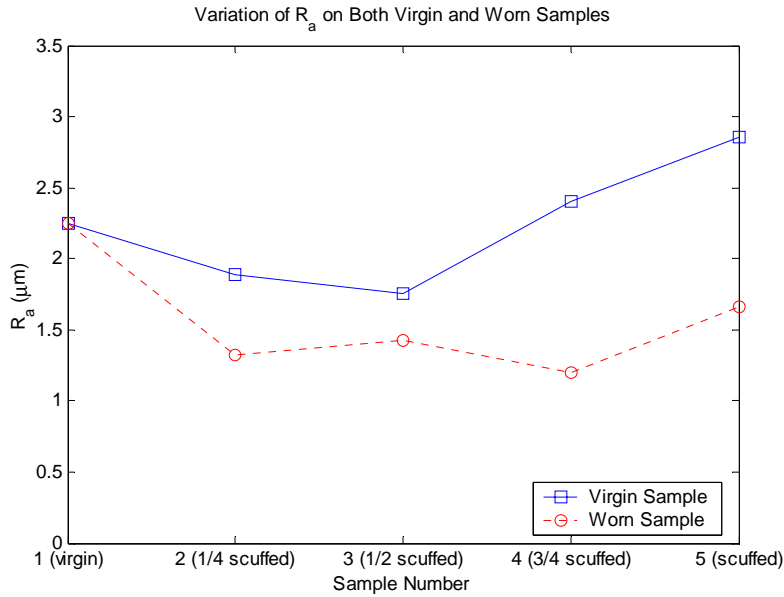
Figure 11. Plot of R_a variation on virgin and worn cast iron disks
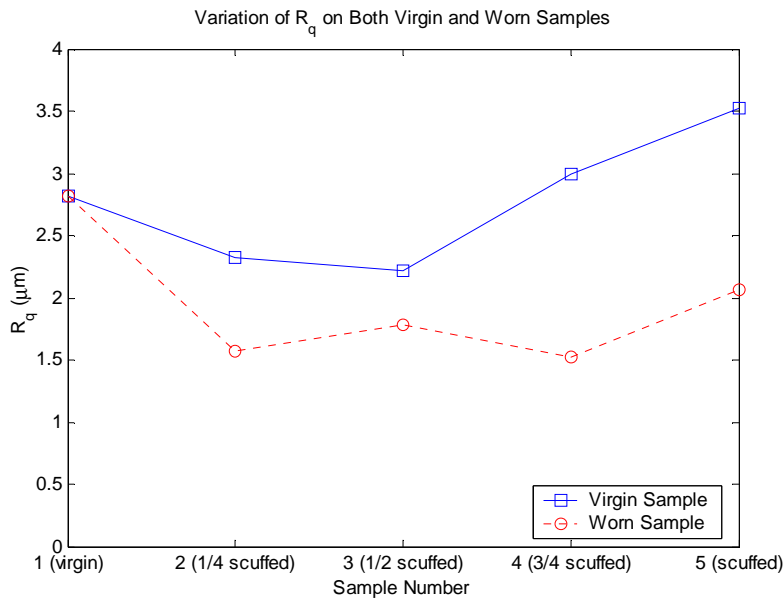
Figure 12. R_q variation of on virgin and worn cast iron disks

3.2.2 Root-Mean-Square (R_q) Trends on Cast Iron Disks

Figure 12 had similar trends as those portrayed in the previous graph, which confirmed that the surfaces here were Gaussian. The general trend in this graph was that as the surface moved from virgin to worn stage the R_q reduced. This reduction came from the fact that the asperities were smoothened thus reducing the roughness. As for

the individual results, the data from the graph suggested an existence of progressive wear of the surface until it finally scuffed.

3.2.3 Average Radius of Curvature of Asperities (R) Trends on Cast Iron Disks

The general trend exhibited by this set of data was that as the surface was worn out, the radius of curvature of the asperities increased. A larger radius of curvature was achieved due to the asperities that were progressively polished out. The conclusion from Figure 13 was that as a surface underwent the evolution of wear, the radius of its asperities increased because the asperities were polished. This supported the information obtained from the R_a and R_q charts.
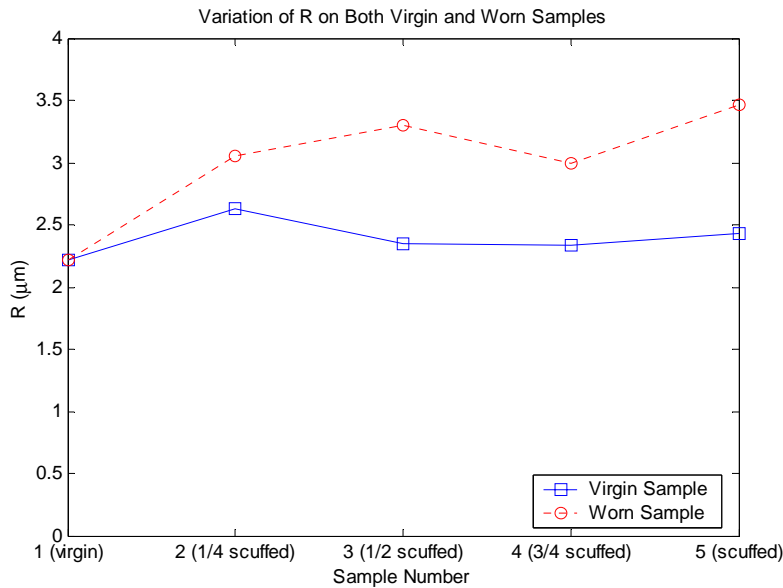
Figure 13. R variation on virgin and worn cast iron disks

3.2.4 Areal Density of Asperities (η) Trends on Cast Iron Disks

This parameter estimates the number of asperities in a given area, and is dependent of the manufacturing process and does not change considerably for minor wear. As shown in Figure 14, the virgin samples had very consistent results as far as the initial density of asperities was concerned. As the surfaces were worn out, the density increased in most cases. This might be contrary to intuition, because as the radius of asperities increased it was expected that the density would decrease. However, as the surfaces were smoothened out, the minor asperities that were not recorded before got counted as asperities now, thereby increasing the count. The scuffed sample showed large decrease in density. However, as mentioned before, this may be due to plastic deformation and other severe forms of surface distress.

13
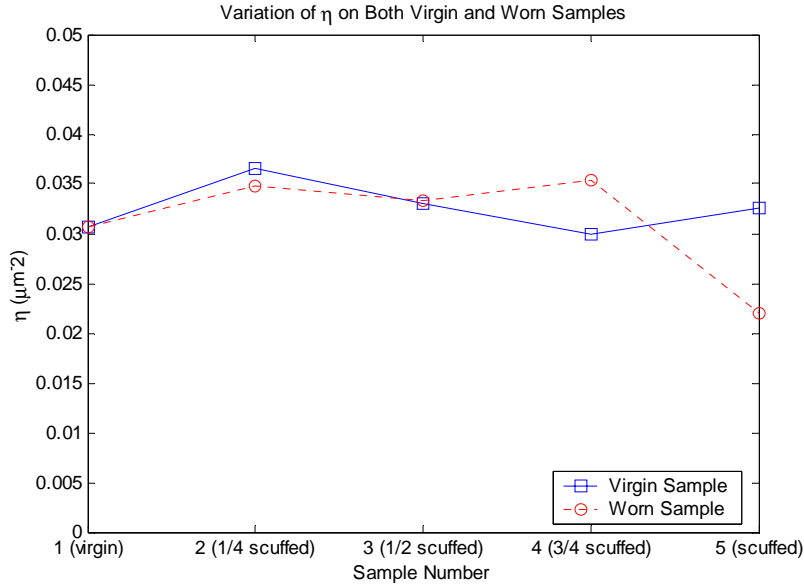
Figure 14. η variation on virgin and worn cast iron disks

3.2.5 Roughness Parameter (β) Trends on Cast Iron Disks

This parameter is the product of η, σ, and R, it is mainly used as a 'check' of the roughness parameters extracted by the analytical methods, and usually ranges between 0.02 to 1.0. The general trend displayed in Figure 15 was that as the surface was worn out, the roughness parameter reduced in value. However this parameter did not give us any new vital information, since it is a product of parameters that have been analyzed before.
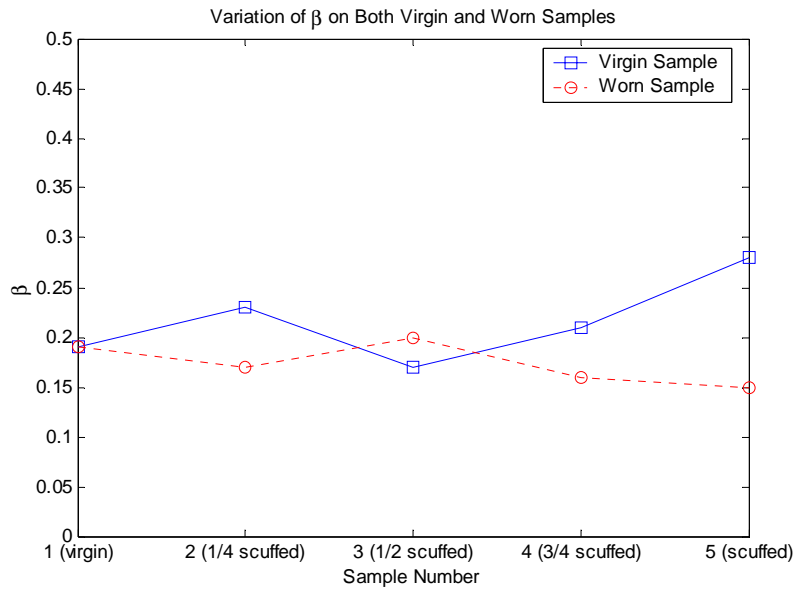
Figure 15. β variation on virgin and worn cast iron disks

3.2.6 Skewness Trends on Cast Iron Disks

Skewness may provide vital information of the shape of the topography height distribution, namely, the degree of asymmetry of surface deviation about the mean. It can also give some indication of the existence of spiky

features (Stout, 1993). In the case of cast iron (Figure 16), the distribution of the virgin skewness parameter was relatively large, thus the changes seen from disk to disk could not hold substantial ground to establish any trends. It should be noted, however, that the skewness did get reduced initially, thereby acknowledging the fact that the asperity peaks were knocked off. The large variation in skewness may be attributed to the rough nature of the cast iron surfaces. Previous studies indicate that with 'regular' mild wear-in, the initial surface begins with a positive skewness (spiky features and machining marks due to machining process). Then, due to plastic deformation, the asperities wear out giving the surface a skewness of about –0.5 (pits and troughs), where the asperities deform elastically. However, this was not the case with these data; instead rather erratic behavior without any marked trends was observed.

3.2.7 Kurtosis Trends on Cast Iron Disks

Kurtosis is the fourth moment of the normalized surface roughness distribution, and is a measure of the peakedness or sharpness of the surface height distribution (Stout, 1993). The general trend in Figure 17 was that the virgin state had a Gaussian distribution ($K \approx 3$). As the sample was worn out the kurtosis became leptokurtic. This graph did not yield any substantial conclusions. This concluded the profilometer data analysis on the gray cast iron.
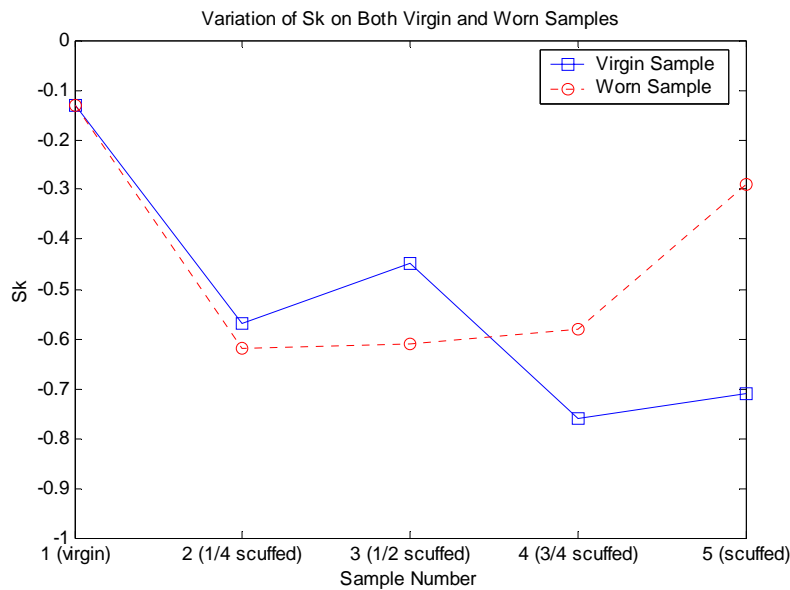
Figure 16. Skewness variation on virgin and worn Iron disks
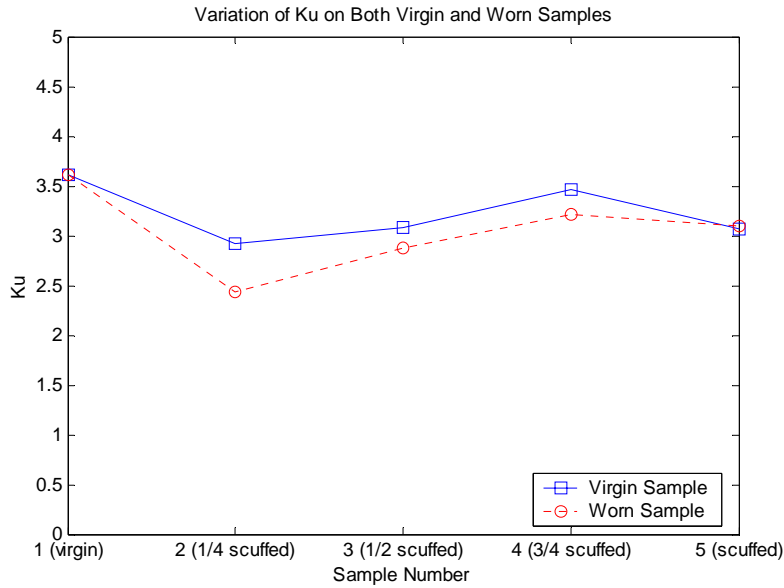
Figure 17. Kurtosis variation on virgin and worn Iron disks

3.2.8 Conclusion on Surface Roughness Analysis on Cast Iron Disks

From the study presented in this section, it was suggested that progressive wear occurred as virgin surface underwent wear, and the asperity peaks were smoothened until scuffing. The profilometer scans and the statistical parameter graphs fully supported this observation. From this chapter it may be supported that smoothening of the surfaces occurred as wear took place, and progressive wear led to scuffing. It should also be noted that compared to the aluminum surfaces, the cast iron surfaces were rougher and harder, thus making it more difficult to establish trends.

3.3 Pin Surface Roughness Analysis

To better understand the contact between the pin and disk, surface data at the pin were recorded and analyzed. Profilometer scans were made on the surfaces of the virgin and worn pins to establish the statistical trends observed due to the geometrical changes. The results of the parameter studies are summarized in Table 2 and discussed briefly in this section.

Table 2. Statistical roughness parameters for steel pins before and after HPT testing

		Pin 1 (Virgin)	Pin 2 (¼ x T_{scuff})	Pin 3 (½ x T_{scuff})	Pin 4 (¾ x T_{scuff})	Pin 5 (T_{scuff})
R_a (µm)	Virgin	3.18	3.19	2.99	2.94	-
	Worn		0.83	0.24	0.47	6.38
R_q (µm)	Virgin	3.83	3.82	3.63	3.58	-
	Worn		1.03	0.32	0.78	7.98
R (µm)	Virgin	11.6	11.1	12.1	12.1	-
	Worn		26.6	62.9	39.8	12.1
η (µm^{-2})	Virgin	4.16 x 10^{-3}	4.45 x 10^{-3}	3.59 x 10^{-3}	3.85 x 10^{-3}	-
	Worn		5.52 x 10^{-3}	9.22 x 10^{-3}	6.26 x 10^{-3}	2.22 x 10^{-3}
β	Virgin	0.19	0.19	0.16	0.17	-
	Worn		0.15	0.18	0.21	0.21
Sk	Virgin	0.12	0.16	0.20	-0.050	-
	Worn		-0.40	-0.81	-2.56	0.0038
Ku	Virgin	2.36	2.19	2.30	2.40	-
	Worn		3.07	6.28	12.03	3.10

3.3.1 Center Line Average (R_a) Trends on Pins

The R_a from sample to sample varied substantially as shown in Figure 18. As a virgin surface was worn out there was plenty of resistance to wear, which was possibly caused by the surface coating. As the surface was further polished, the R_a reduced as seen with the disk data in the previous chapter. At ¾ x T_{scuff} the R_a remained similar to that of the previous stage. At scuffing the R_a increased drastically, primarily due to plastic deformation. All the results seen here were as expected.
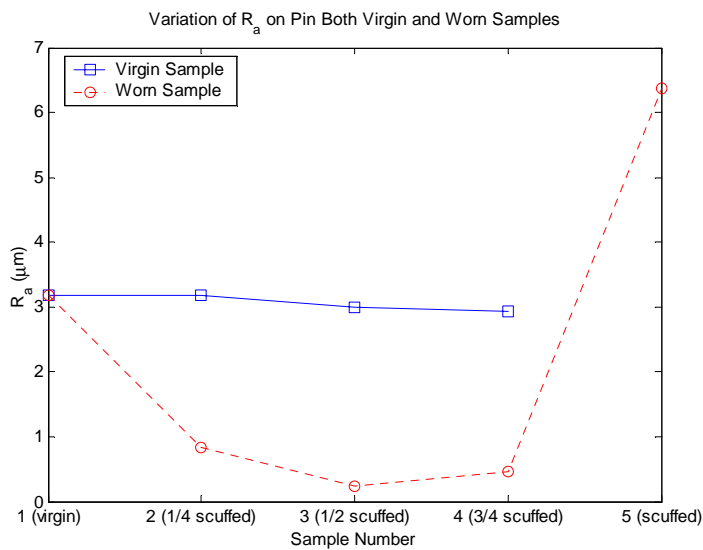
Figure 18. Plot of R_a variation on virgin and worn pins

3.3.2 Root-Mean-Square (R_q) Trends on Pins

The R_q of the sample showed clear trends of reduction in value due to polishing as expected. As displayed in Figure 19, the R_q values were relatively constant initially. However, in general, as the surface was worn out, the R_q reduced. At scuffing the R_q increased due to plastic deformation. The R_q pin trends were similar to those seen at with the disks, the only notable difference being that scuffing on the pin causes greater damage then that on the disk.
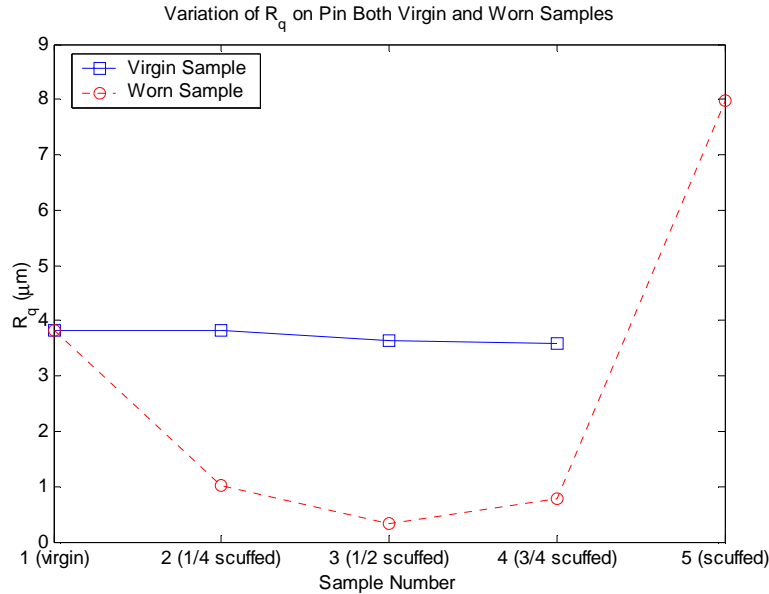
Figure 19. R_q variation of on virgin and worn pins

3.3.3 Average Radius of Curvature of Asperities (R) Trends on Pins

This set of data indicates that as a surface is polished, the radius of asperities increases. As seen in Figure 20, the initial radius of asperities was relatively constant indicating that the pins were indeed machined in a similar manner. As the surfaces were polished, the radii of the asperities increased. At ½ x T_{scuff}, the radius was much higher than the rest. This may be due to the limited experiments performed, possibly making that the data point invalid subject to experimental error. However it was interesting to note that the final radius was similar to the virgin radius.

3.3.4 Areal Density of Asperities (η) Trends on Pins

As a surface underwent wear, minor asperities emerged on the on the surface, thus increasing the density of asperities. This trend was noted in Figure 21. However, at ½ x T_{scuff}, the density increased sharply. It was suggested that this point be ignored and to be accounted for as an experimental error. An interesting thing to note was that the density of the scuffed surface was less than that of the virgin surface.
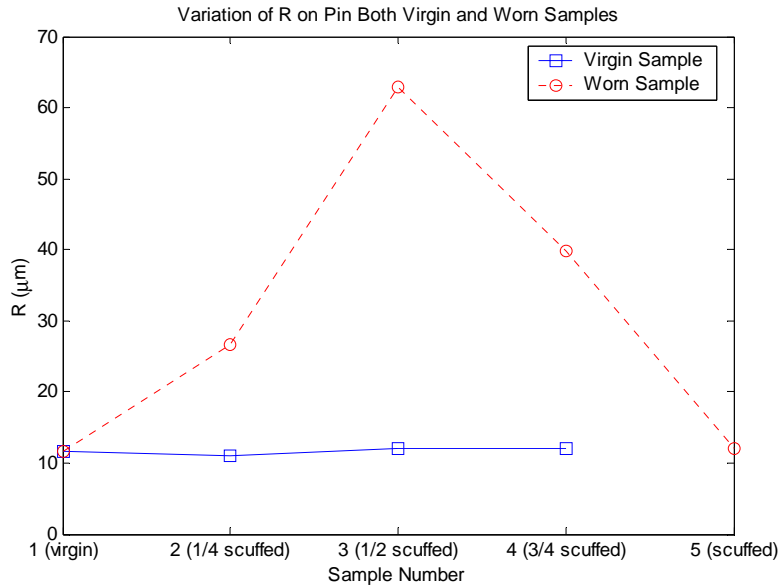
Figure 20. R variation on virgin and worn pins
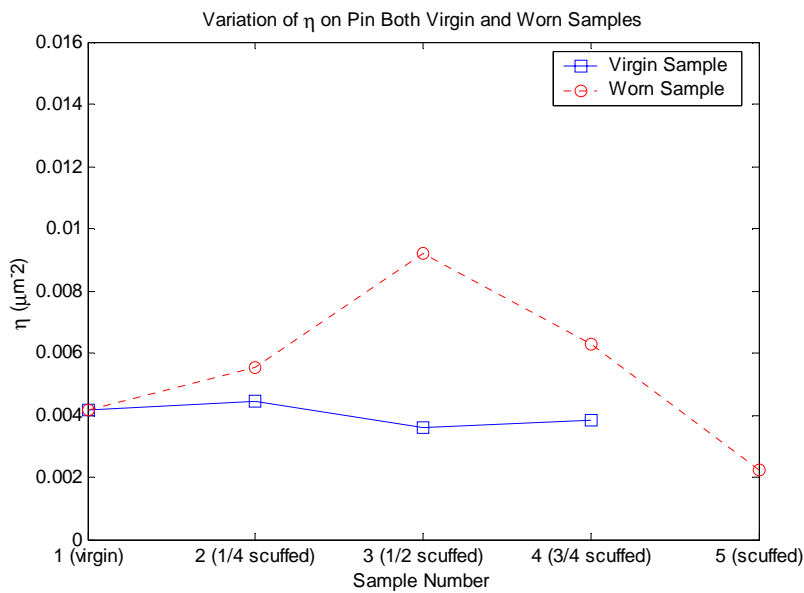
Figure 21. η variation on virgin and worn pins

3.3.5 Roughness Parameter (β) Trends on Pins

This parameter is a check for the data extracted from the analytical analysis, and is values are expected to range between 0.02 and 1.0. The results tallied with these expectations, as shown in Figure 22. The only difference arising between the data on the pin and disk was that the β value of the worn surface generally decreased in the disk, while in the pin the opposite occurred.
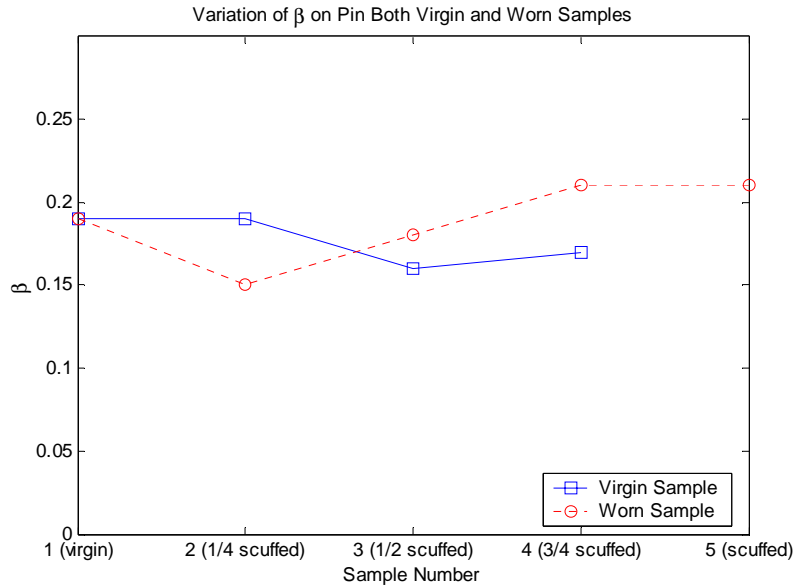
Figure 22. β variation on virgin and worn pins

3.3.6 Skewness Trends on Pins

Skewness was by far one of the most important parameter in statistical analysis. Figure 23 shows that the initial surface had a slightly positive skewness indicating that the surface was dominated by peaks. As the surface was worn out the skewness reduced in values, suggesting that the peaks had been polished out and the valleys dominated the profile. It should be noted that at scuffing the skewness was similar to that of the virgin surface. One of the interpretations of this wais that the pin got "re-machined" by the disk.
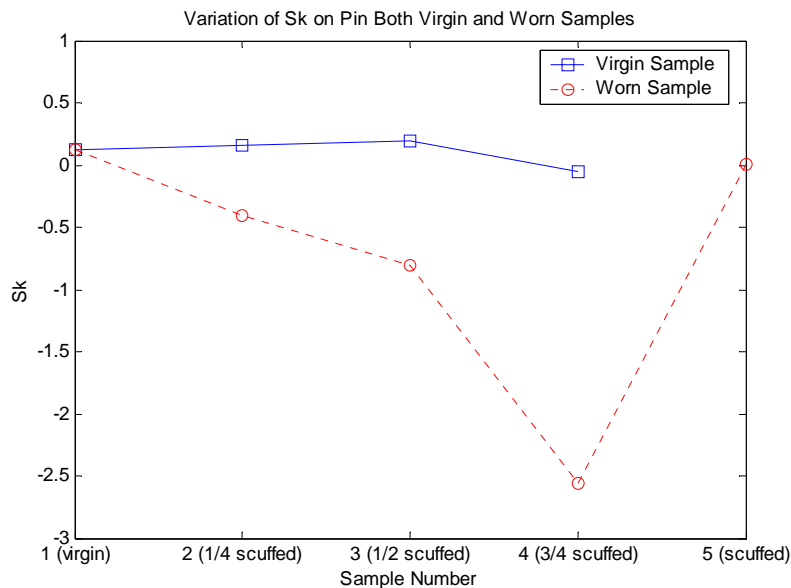
Figure 23. Skewness variation on virgin and worn pins

3.3.7 Kurtosis Trends on Pins

Figure 24 shows that the virgin surface was Gaussian ($K \approx 3$). Not much was revealed from the worn surface, thus the data did not yield any substantial conclusions.
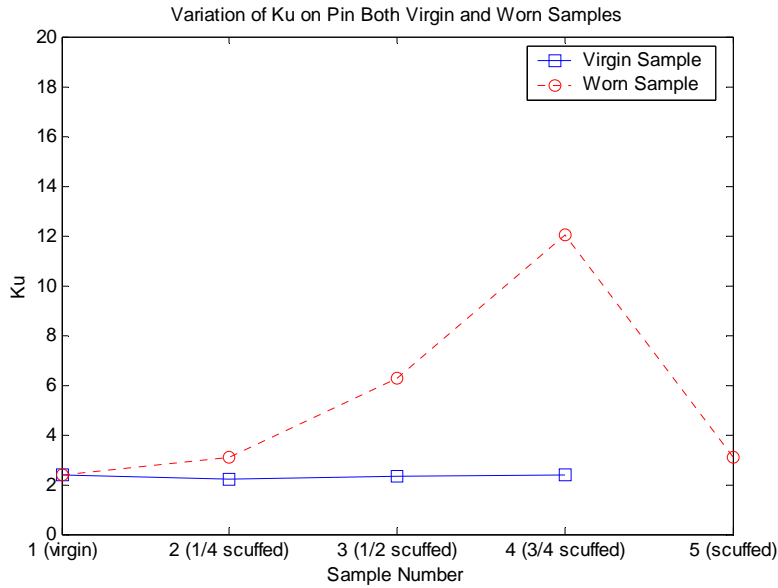
Figure 24. Kurtosis variation on virgin and worn pin

3.4 Conclusion on surface roughness analysis

In this chapter, surface roughness parameters for both the pin and disk surfaces were calculated, whose values were then compared in between wear stages as well as between virgin and wear states. Both sets of data revealed anticipated results, although some notable points arose. From the pin analysis it was observed that wear on the pin was greater than that of the disk, possibly suggesting that the non-contacting surface played a role in wear. Next observation was that the pin at the end of wear seemed to return to its original statistical surface properties, indicating that it was worn to the point that it took an imprint of the disk machining marks to generate a new consistent surface. To further explore and support these observations, it was suggested that the HPT tribological experiments be repeated to focus on the aforementioned points.

Chapter 4. Micro-structural Analysis

4.1 Introduction on Scanning Electron Microscope (SEM)

Before analyzing chemical compositions and material properties of gray cast iron, it may be of special interest to examine closely the top virgin surface microstructure of the sample. This may later provide useful insights into any findings related to progressive, subsurface-level changes accompanied by wear-scuffing mechanism. The electron microscopy is an existing inspection tool which utilizes x-ray diffraction. The scanning electron microscope (SEM) in particular obtains structural images by the strength of the beam of secondary electrons ejected from the sample surface when a small electron beam spot ($< 1\mu$m in diameter) is scanned over the surface area. The advantage of using the SEM comes from its magnification, which is considerably better than the conventional optical microscope. High magnification with the "depth of field" capability is particularly useful in looking for grain structures and boundaries. Important surface irregularities such as fracture features can also be inspected by the SEM.

The SEM technique, however, requires a "flat, polished" surface to reveal its main microstructure. In addition to the surface polishing, a method of chemical etch must be performed to display grains and grain boundaries by allowing different grains and grain boundaries to dissolve at different rates (Pergande, 2001). A standard 10-step polishing procedure, originally based on a technical note by Buehler Inc., was adopted to polish the gray cast iron sample (Vander Voort, 1999). A similar polishing procedure had been used in aluminum alloy polishing previously (Pergande, 2001). The polishing procedure was as follows;

1.) On a small cut virgin iron sample, polish with 400-grit paper until all original scratches (e.g. machining marks) are removed. Because the original surface roughness is of the order of 2 µm (i.e. rough), polishing with coarser grit paper (320-grit or less) may be necessary. A water stream is used to carry particles away from the specimen. Avoid grinding the sample in back and forth directions, which would form the surface "bowed" instead of flat. Rather, polish the surface only in one specified direction, preferably in outward motion, or in the direction perpendicular to machining marks.

2.) Polish with 600-grit paper until all original scratches from 400-grit paper are removed. A water stream is used to carry particles away from the specimen.

3.) Polish using 9 µm METADI® solution on nylon cloth at 110 rpm for 5 minutes (or until all scratches from 600-grit paper are removed). Make sure the polishing surface created by nylon cloth and polisher is as flat and free of water bubbles as possible, for this would result in non-uniformly polished sample surface. Depending on the direction of rotation of the polisher (CCW), simultaneously rotate the sample in a small circle in the direction opposite to that of the polisher (CW).

4.) Polish using 3 µm METADI® solution on nylon cloth at 110 rpm for 3 minutes (or until all scratches from 9µm METADI® solution are removed). Depending on the direction of rotation of the polisher, (CCW) simultaneously rotate the sample in a small circle in the direction opposite to that of the polisher (CW).

5.) Polish using Mastermet® Colloidal Silica Polishing solution (0.06 μm) with Mark V Lab Alpha A Cloth® at 90 rpm for 2 minutes (until smooth).

6.) Gently clean sample with a cotton swab soaked in de-ionized water.

7.) Remove acetone residue with a cotton swab soaked in ethanol.

8.) Dry using air hose.

9.) Chemically etch with a 2 % Nital solution for approximately 10 seconds. Wipe on etch in one direction using a solution-soaked cotton swab. If the etch is left on for too long of a time, it will 'burn' the sample.

10.) Clean with acetone, then ethanol, and dry appropriately.

Once the sample has been properly polished and etched, it is ready for inspection inside the SEM vacuum chamber.

4.2 Surface / Bulk Microstructure of Gray Cast Iron

A ferrous alloy such as gray cast iron has been studied to great extent, and much about its microstructure is well documented in the material property literature. Generally, cast irons are defined as the ferrous alloys with greater than 2 wt % carbon and 3 wt % silicon for control of carbide formation kinetics (Shackelford, 1988). Gray cast iron is a type of cast iron, whose carbon and silicon contents may vary between 2.5 and 4.0 wt % and 1.0 and 3.0 wt %, respectively (Callister, 1997). Cast iron is formed by pouring molten metal into a specified shape of mold then cooled. It generally has inferior mechanical properties compared to *wrought* alloys. Cast iron has a fairly non-uniform microstructure with some porosity, yielding its microstructure to be comparatively weak and brittle in tension. However, strength and ductility are generally known to be much higher under compression. Due to its relatively high damping capacities and its low cost, gray cast irons are largely used in many engineering applications exposed to heavy vibrations.

Microstructures for most gray cast irons consist of dark graphite existing in the form of flakes, which reside inside an α-ferrite or pearlite matrix. Figure 25 shows a typical microstructure of gray cast iron (100 ×) where dark graphite flakes are surrounded in a matrix of 20 % free ferrite (light constituent) and 80 % pearlite (dark consitituent) (Shackelford, 1988).

Figure 25. Typical microstructure of gray iron (100 ×), dark graphite flakes in a surrounding matrix of 20 % free ferrite (light constituent) and 80 % pearlite (dark constituent) (Shackelford, 1988)

Because of the nature of polishing procedure, which alters top surface roughness and eliminates top layers of materials, only one virgin sample was prepared and used to examine the top surface microstructure. The gray cast iron sample was cut into a small rectangular piece (7 mm x 10 mm) approximately 3 mm in thickness, and put inside the SEM system after the polishing/etching as previously specified.
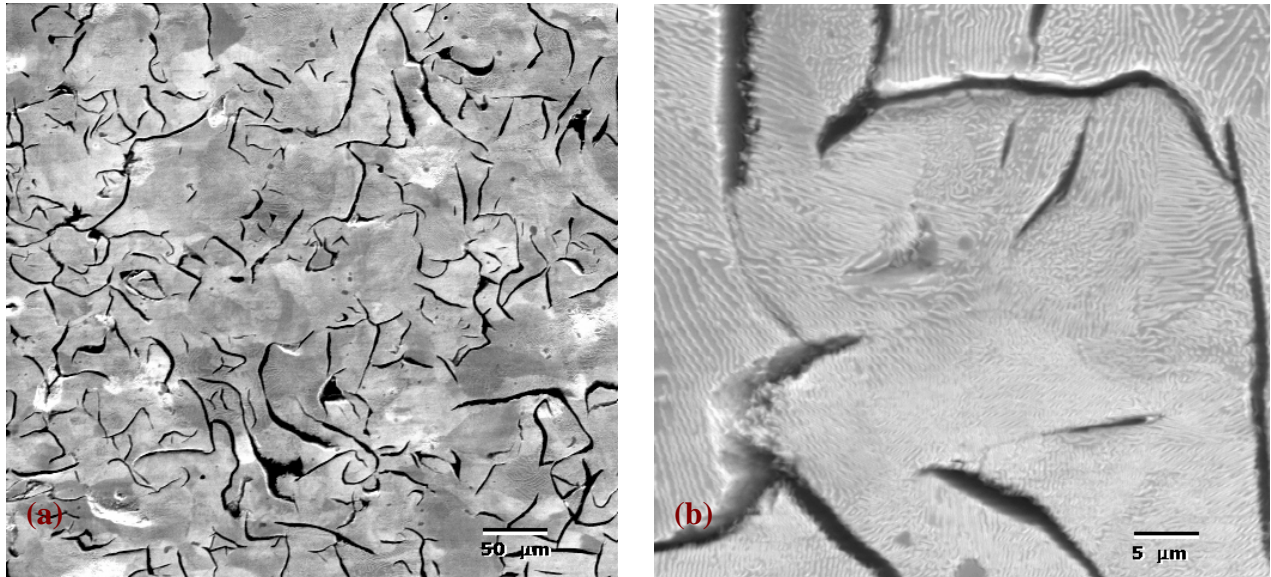
Figure 26. Microstructure of polished gray iron taken by the SEM at (a) 500 × (b) 2000 × magnifications, respectively

Figure 26 shows top microstructure images (taken at 500× and 2000× magnifications) of the polished gray cast iron sample prepared originally for the HPT tribological testing. As seen in the figure, the gray cast iron used in the experiment consists of similar microstructural constituents to those found in a typical gray cast iron, e.g. Figure 25. Clearly, dark string-like materials represent graphite components evenly dispersed throughout the surface,

surrounded by what seems to be a mixture of light ferrite and dark pearlite matrix, whose exact corresponding percent compositions are however unknown. The formation of graphite depends on the cooling rate and the existence of silicon during solidification, and graphite promotes high strength (20 GPa in tensile) (Callister, 1997). When the same image was zoomed into 2000× magnification (Figure 26(b)), greater details on the substrate matrix were revealed. At the higher magnification, the alternating layers of two phases, α-ferrite and pearlite, became evident as thick light layers and darker colonies of layers oriented in the same direction, respectively. Ferrite has the soft, ductile properties, whereas pearlite has the intermediate properties between ferrite and cementite (i.e. hard, brittle) (Callister, 1997). Although some porosity on the microstructure was anticipated, no apparent visible indication of porosity was captured in the SEM images.

4.3 Conclusion on Microstructure

Using the conventional polishing and etching techniques specified for observing the microstructure of cast iron, "bulk" microstructures of the gray cast iron sample were observed and analyzed in this section. Because the microstructure becomes visible only after performing carefully conducted multi-step polishing/etching procedures, which eliminate several micro-meters of top layers, the image captured under the SEM is the "bulk" structure of the gray cast iron. Unlike the microstructure seen in, for instance Al390-T6 samples (Pergande, 2001), no well-defined grains or grain boundaries were observed in the gray cast iron sample. However, random, non-uniform graphite components residing inside ferrite-pearlite matrix was detected based on a comparative analysis to the microstructure image available for an existing gray cast iron. Although the gray cast iron is generally "harder" and "stronger" than conventional metals (considering its relatively simple manufacturing procedure and low cost), the "weak" and "brittle" (bulk) nature was suggested by the visual observation of its fairly non-uniform microstructure despite the presence of graphite. Although some general conclusions on its bulk microstructure may be made based on the SEM images, both its qualitative and quantitative material properties could not be extrapolated from the visual observations alone. More exhaustive studies on chemical compositions and material properties must be done individually using other techniques, which became the main focus of the next two chapters.

Chapter 5. Nano-scale Surface and Sub-Surface
Chemical Analysis of Cast Iron

5.1 Introduction on Auger Electron Spectroscopy (AES)

As the iron surface undergoes various wear stages leading to scuffing, changes occurring on the surface do not merely bring about the change in the surface topography. It may also imply significant changes in material properties, such as changes in chemical composition of materials throughout the wear evolution until onset of scuffing. This is due to the high pressure and temperature involved during scuffing phenomena, which usually alters the material properties significantly from the virgin state. The purpose of this section is to investigate various changes appearing in chemical compositions, mainly on the sub-surface at the nanometer scale. One method of chemical analysis chosen for this study is the Auger Electron Spectroscopy (AES), which in turn can provide important information about the atomic concentration of elements within the sample as a function of depth. Based on the previous studies done by Patel (2001) on the surface of aluminum alloy, it was decided that the AES chemical analysis may shed insights to fundamental wear mechanisms. Refer to Patel (2001) for more on the background information on the operational mechanisms of Auger Electron Spectroscopy.

The AES utilizes the Auger effect in which Auger electrons are produced when incident radiation interacts with an atom with the energy necessary to remove an inner shell electron from the atom. This interaction leaves the atom in an excited state with a core hole, resulting in the emission of an electron known as Auger electron. The AES system is equipped with the electron spectrometer, which captures various components of atoms sputtered from the surface of the sample as a function of sputter depth (with a known sputter rate). One main drawback for using the AES techniques is that it is insensitive to certain atoms including hydrogen and helium, as well as all elements. If one is to investigate chemical <u>compounds</u> of a given surface, an existing method such as the X-ray Photoelectron Spectroscopy (XPS) technique may be desirable. Another important fact to keep in mind when performing the AES analysis is to be able to look for presupposed atoms that may exist on the material surface. In this study, eight major atomic components were specifically searched for and analyzed, as listed in the table below;

Table 3. Searched chemical elements from the AES analysis of the gray cast iron

Iron (Fe)	Carbon (C)	Oxygen (O)	Manganese (Mn)	Nickel (Ni)	Nitrogen (N)	Phosphorus (P)	Chlorine (Cl)

Note that there also existed layers of a lubricant coating protecting the top surface of gray cast iron samples. Therefore, the searched chemical elements also may relate to the chemical composition of the lubricant coating applied to the cast iron samples. A compliant type of lubricant that is strongly acidic known as Parco® Lubrite 2 was used for coating. The coating thickness was estimated to range from 0.2 to 0.4 mil or 5 to 10 µm. The AES analysis should account for the coating composition as well as the cast iron sample surfaces.

5.2 AES Experiments on Cast Iron Samples

The cast iron samples after the HPT tests were carefully cut into small pieces using a low speed diamond saw in preparation of the AES experiments. Since any surface contaminants (e.g. fingerprints, dust, etc.) existing on the sample surfaces may affect the sputter process, these pieces were then ultrasonically cleaned in acetone and rinsed in ethanol. The residual ethanol was then hot air-dried off the sample surface. The chosen sputter rate was

established to be approximately at 12.2 nm/min. This sputter rate was kept constant for each of the 5 test iron samples. Accurately profiled sputter rate is critical when converting the data into depth profiles (in nm), as it relates to the changes in chemical composition of the surface moving into the sub-surface of the sample.

5.2.1 Sample by sample AES analysis

Two methods are available upon analyzing the AES data, the first being the depth profiles relative to intensity from the AES, and the second being the depth profiles relative to atomic percentage concentration. Only the latter analysis was discussed in this section from the virgin sample to scuffed sample, each concerning percent atomic concentration relative to each other. Figures 27 to 31 display atomic percentage from the AES for each of the 5 test iron samples.

As expected, the virgin sample was highly concentrated on iron as the sputtering depth was increased into 50 nm or more, as shown in Figure 27. However, the carbon and oxygen elements initially displayed highest percentage, while the iron percentage started increasing rapidly from a very low concentration level. The existence of fairly high concentration of oxygen (≈ 20 %) indicated the existence of oxide layer(s) usually found in the top layer surfaces as the results of oxidation. A constant oxygen concentration displayed for the depths of 50 nm or above may be due to the oxygen compositions found together in other chemical compounds. Carbon reduced at a fast rate down to about 70 nm, from which it remained fairly constant. Although manganese compound was specified to be a major component of the lubricant coating (20-40 % of the whole lubricant), its percentage throughout the sputter depths was comparatively low, ranging below 10 %. Other atomic components such as nickel, nitrogen, phosphorus, and chlorine were found in very small traces, and may be insignificant.
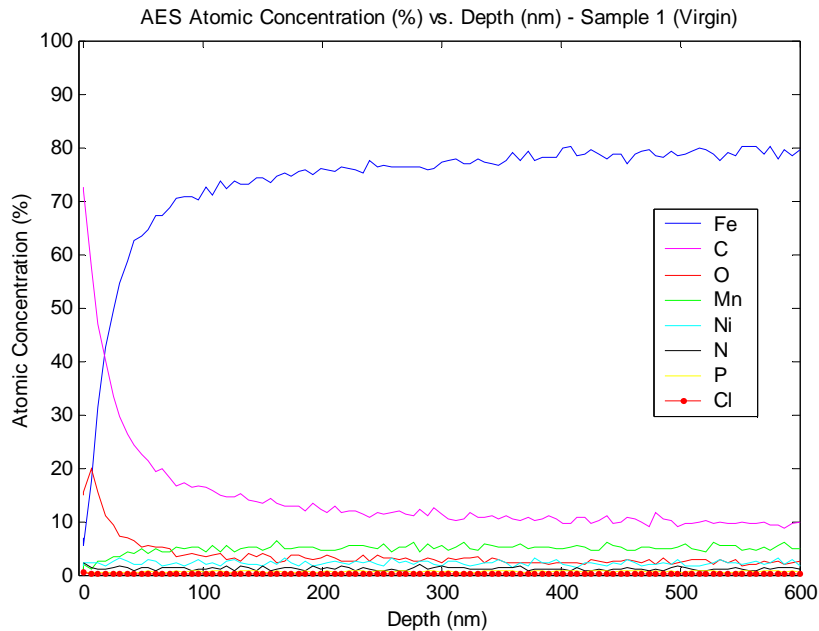
Figure 27. Percent atomic concentration on Sample 1 (Virgin)

Figure 28 displays the relative percentage of the atomic concentration on Sample 2, or the cast iron sample after ¼ x T_{scuff}. By the overall account, the entire trend closely resembled that of the virgin sample. One essential difference from the virgin sample was that the rate of increase or decrease of major atoms at the uppermost depth

(20 nm or below) was much faster for the ¼ x T_{scuff} sample. Oxygen concentration decreased much faster for the depth of 10 nm or more, indicating that the thickness of uppermost oxide layer may have decreased due to wear. However, note that the initial oxygen concentration was higher ($\approx$ 35 %) for this sample than that for the virgin sample ($\approx$ 20 %). This may indicate that the degree of oxidation was affected by wear. Similarly, the carbon concentration decreased much faster than before, signaling its transition to more drastic alteration of the surface chemical composition for progressive wear stages.

AES Atomic Concentration (%) vs. Depth (nm) - Sample 2 (1/4 x T_{scuff})
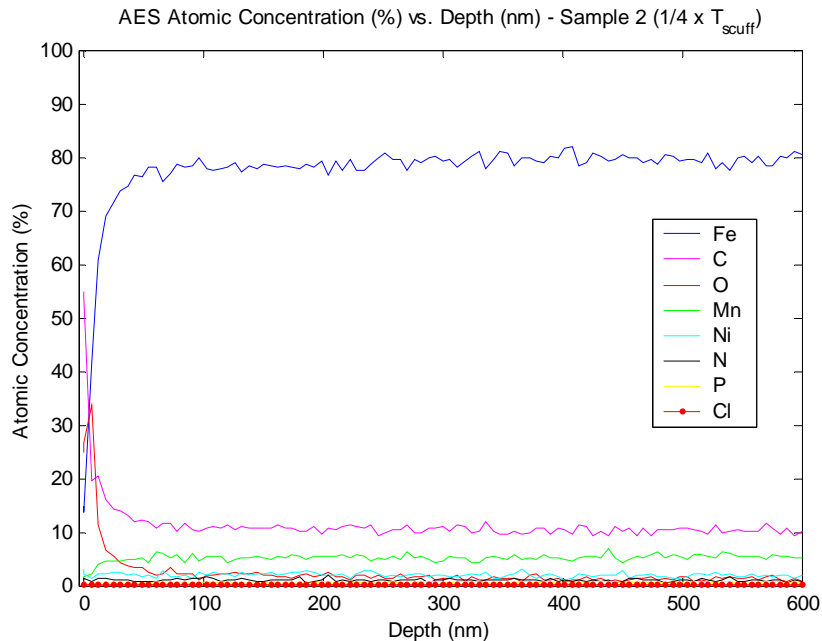
Figure 28. Percent atomic concentration on Sample 2 (1/4 x T_{scuff})

In the ½ x T_{scuff} sample, more drastically different changes in atomic concentration started to emerge, although the general trends were still similar to those from the two previous stages (Figure 29). Unlike the previous stage, however, the iron and carbon elements took comparatively longer to reach steady-states. Furthermore, the oxygen components seemed to decrease at a slower rate than at ¼ x T_{scuff}. All the other remaining atomic components did not seem to vary, creeping at very low concentration levels as before.

At ¾ x T_{scuff}, the surface appeared to be beginning to prepare for failure. However, from the AES data it was difficult to observe any marked difference in trends at this stage as captured in Figure 30. The carbon element seemed to start at higher concentration initially, but again decreased rapidly and finally reached a steady state of about 20 % after the depth of 100 nm or above. The peaky behavior in the oxygen compound at a shallow depth appeared to be less apparent compared to the previous wear stages, nevertheless it decreased to a very low level after 150 nm sputter depth or above.
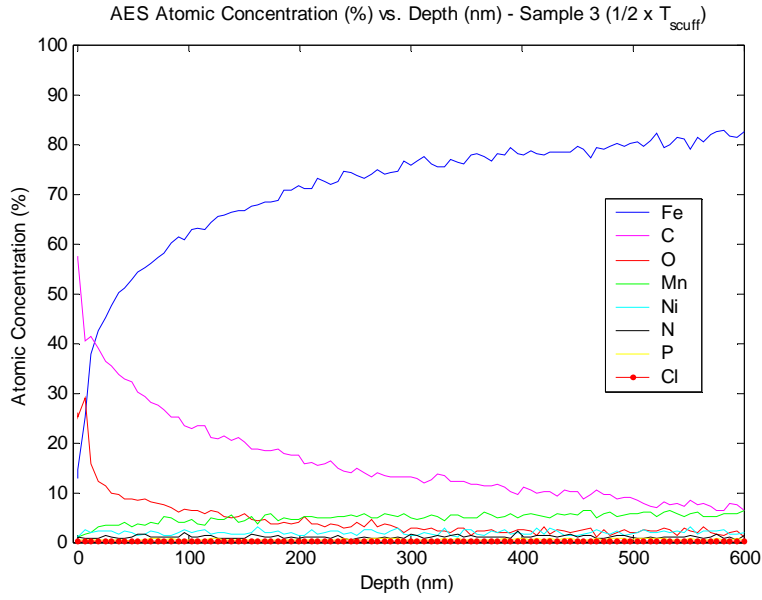
Figure 29. Percent atomic concentration on Sample 3 (1/2 x T_{scuff})
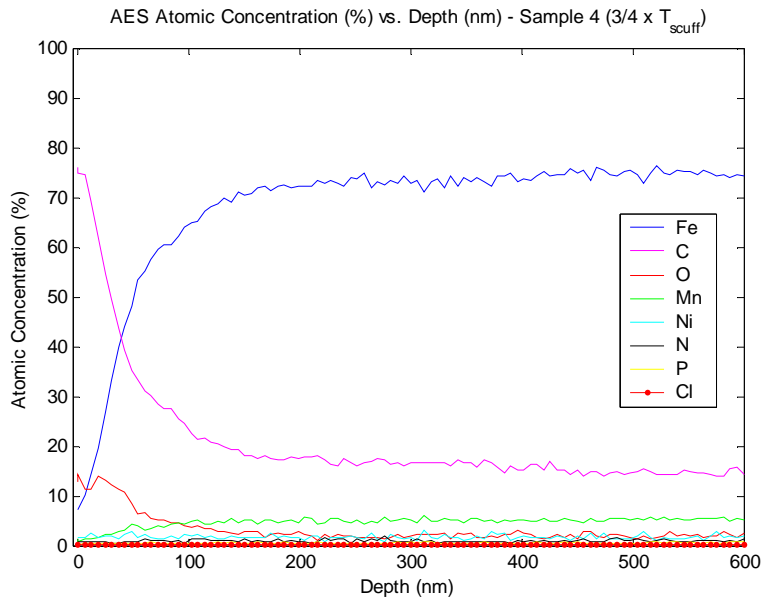
Figure 30. Percent atomic concentration on Sample 4 (3/4 x T_{scuff})

At T_{scuff}, previously seen trends seemed to have been lost, indicating a complete alteration of the chemical composition of the surface accompanied by the onset of scuffing (Figure 31). One major observation made at scuffing was a severe depletion of iron compared to the prior wear stages. The highest atomic concentration shown below 250 nm sputter depth was the oxygen, varying between 50 to 35 %, which indicated severe oxidation. Although iron and carbon concentrations were steadily increasing, scuffing appeared to be associated with the most amount of change in concentration of the oxide layers. Manganese concentration appeared to have decreased from before, indicating the loss of lubricant coating at scuffing.

29

AES Atomic Concentration (%) vs. Depth (nm) - Sample 5 (T_{scuff})
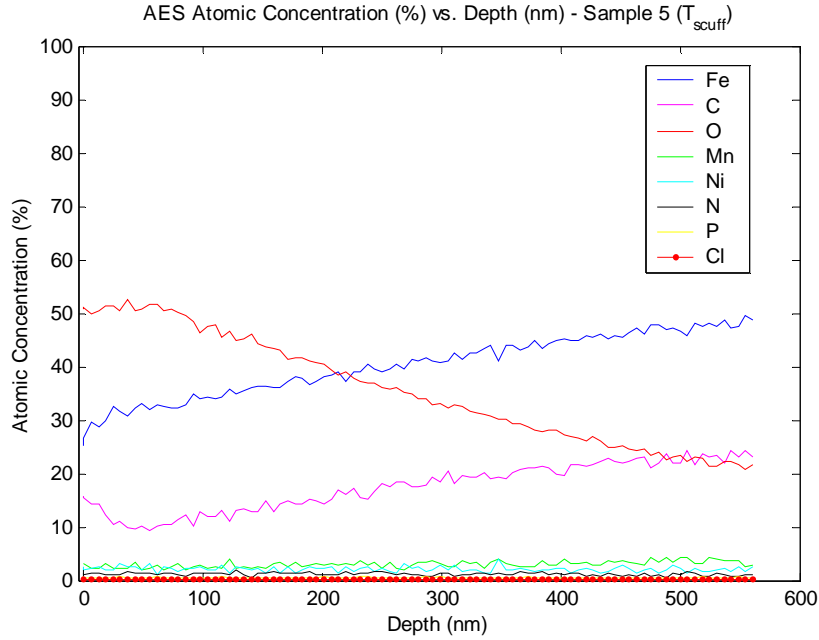
Figure 31. Percent atomic concentration on Sample 5 (T_{scuff})

5.2.2 Element by element AES analysis

   To investigate the details of each atomic component at each wear stage, atomic percent concentrations of all five samples were plotted together as a function of depth.

   Figure 32 displays a decrease in concentration of iron at ½ x T_{scuff} and a drastic reduction at T_{scuff}. However, at ¼ x T_{scuff}, the initial iron concentration and the rate of its increase was much higher than at other wear stages. The erratic behavior at ¼ x T_{scuff} was also previously remarked in the surface roughness analysis.

Variation of Fe with wear evolution
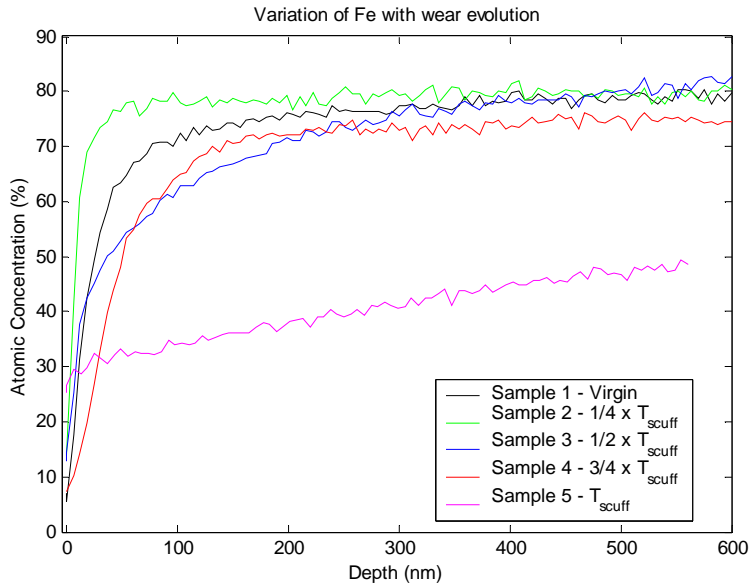
Figure 32. Variation of Iron with wear evolution
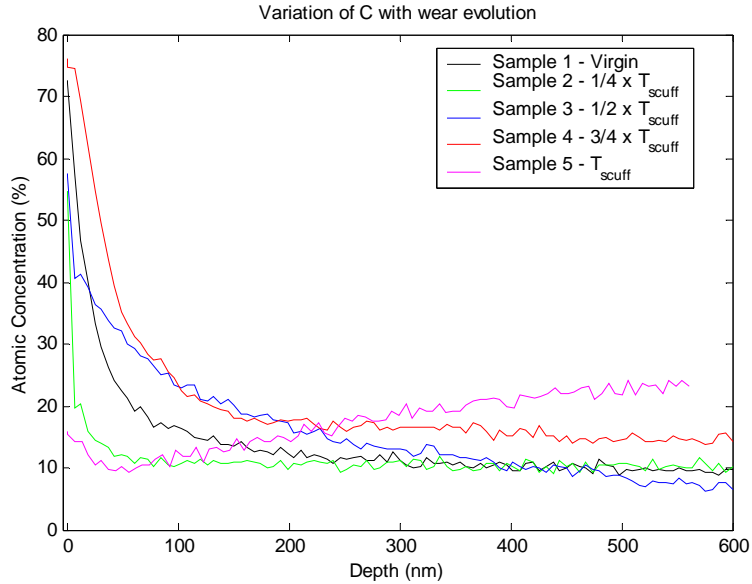
Figure 33. Variation of Carbon with wear evolution

Figure 33 shows the variation of carbon with wear. Although some differences in the rate of drop in carbon concentration existed in the first 100 nm layer, the only noteworthy difference was seen at T_{scuff} only. While all the wear stages prior to scuffing eventually reached a steady-state carbon concentration of about 10 % (it would eventually grow to higher percentage when the bulk was reached), carbon concentration slowly crept up at scuffing. This was because scuffing removed significant amount of material, thereby destroying the protective uppermost surface layer, making the bulk closer (high in carbon).

Figure 34 delineates the oxygen component compared at all wear evolutionary stages. Although no definitive trend could be established from this plot, one may conclude that the oxide layer(s) as indicated by the oxygen concentration was indeed influenced by wear phenomena (i.e. peak levels and the rate of decrease were different initially). When the surface was scuffed, the level of oxygen concentration was almost 50 % of the entire atomic concentration, implying the amount of change on the surface was quite exorbitant not only what was seen in its top surface geometry (i.e. surface roughness) as previously studied, but also in its entire subsurface chemical element composition (i.e. heavy oxidation).
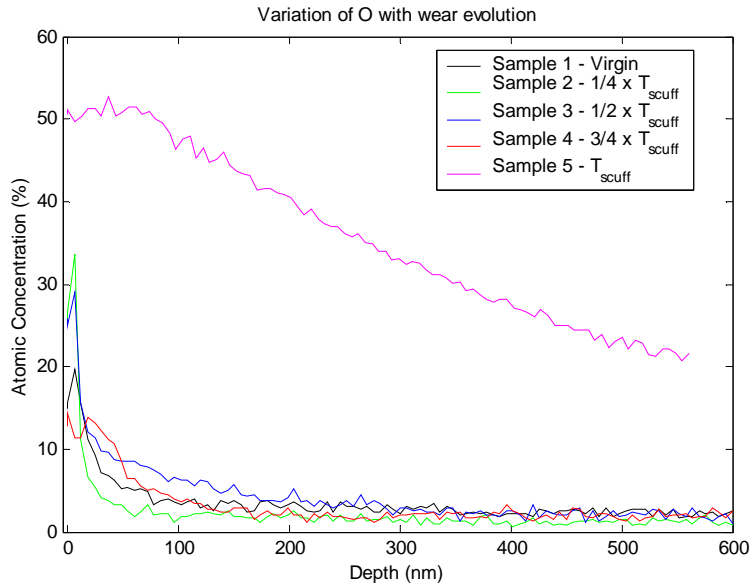
Figure 34. Variation of Oxygen with wear evolution

When the manganese concentration at each wear stage was plotted and zoomed in for better observation, Figure 35 resulted. Behavioral distinction between each wear stage was quite difficult to make, except at T_{scuff}, in which the manganese concentration was nearly halved from the previous samples. As explained earlier, this dramatic decrease of manganese at T_{scuff} was due to the depletion of top lubricant coating by the damage incurred by scuffing.
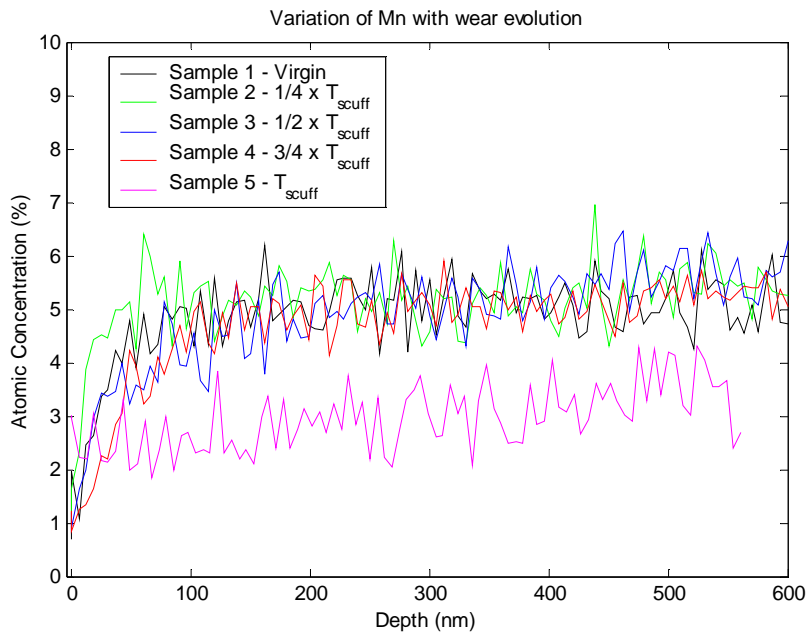
Figure 35. Variation of Manganese with wear evolution

For all the other chemical element compositions such as nickel, nitrogen, phosphorus, and chlorine, no significant variation or trend was observed in between each wear stage. Figure 36 shows the variation of their

chemical compositions as the surface experiences more wear up to the point of scuffing. As soon as wear was initiated, chlorine, however, seemed to decrease in its concentration from the virgin in the first 50 nm, as depicted in Figure 36(d).
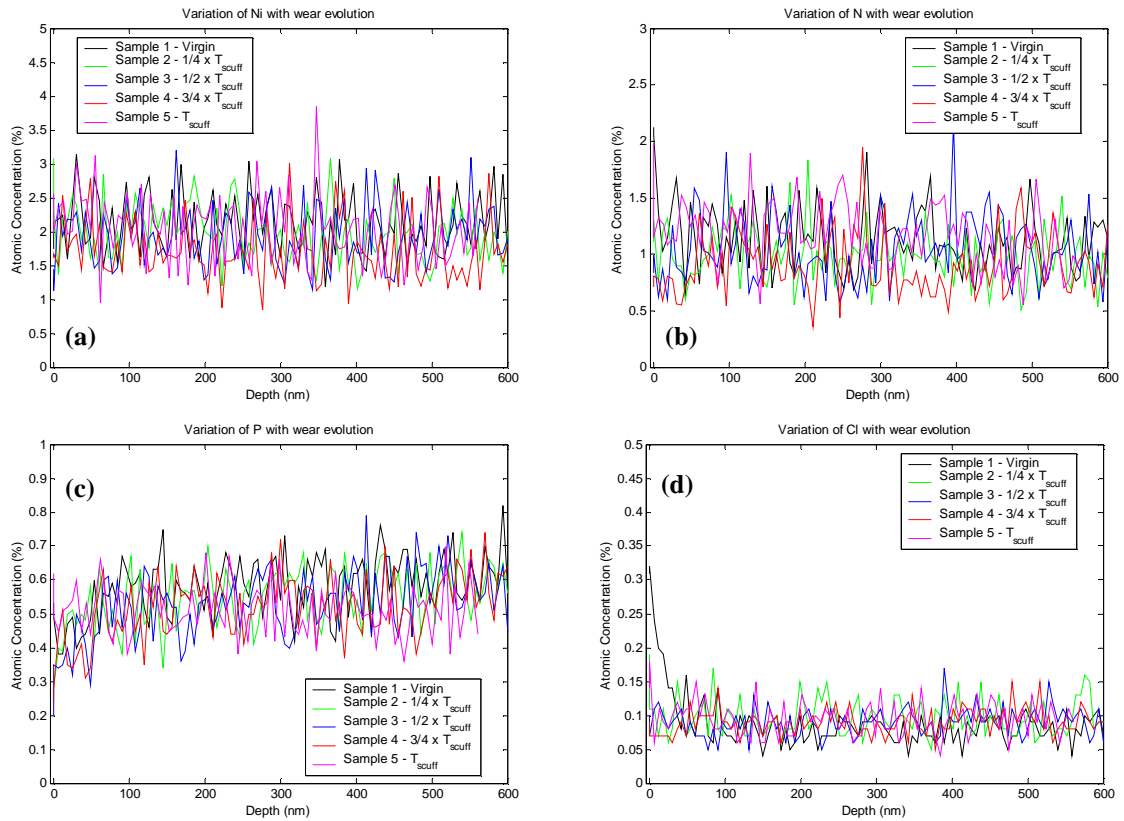
Figure 36. Variation of (a) Nickel, (b) Nitrogen, (c) Phosphorus, and (d) Chlorine with wear evolution

5.3 Conclusion from AES Analysis

Though it was initially hypothesized that the AES techniques may result in progressive capture of alteration in chemical element composition as the surface went through the tribological wear stages, this did not seem to be the case in this study. Perhaps the inherent chemical composition of the cast iron sample used in these experiments may be of those that cannot be optimally captured by the AES analysis. Furthermore, vast majority of chemical elements for the gray cast iron may exist in "compounds", which share most of the same atoms within their chemical bonds, thereby greatly "averaging" the atomic concentration analysis. The XPS tests may be able to provide more valid information on chemical composition of the cast iron samples by detecting chemical bonding information. One other atomic element that was overlooked and left out during the AES experiment is silicon. Because graphite formation is generally promoted by the presence of silicon in concentrations great than 1 wt %, it may have revealed potentially significant information about changes in chemical composition of the surface material as it experiences more wear.

Throughout the depth profiling analysis, no earmark trends were observed with wear evolution that led to scuffing. The most amount of change in the chemical composition was observed at T_{scuff} and not so much at each wear stage, which may not be of practical interest since the surface has already failed at scuffing. Surprisingly, even

the iron concentration did not yield any discernable change between progressive wear stages, except at T_{scuff}, in which the iron concentration decreased drastically. The change of the oxide layer and degree of oxidation can be derived from the oxygen concentration plot, and from the two different rates of decrease seen at shallow depths (100 nm or below), there may exist two different oxides (Patel, 2001).

Chapter 6. Macro-, Micro-, Nano- Hardness Tests

6.1 Introduction

As more insights are gained from recent hardness tests reported at various scales, several hardness test techniques are adopted and explored in this section to establish the change in hardness from macro- to micro- level, and further down to nano-scale. From the previously reported experimental case on Al390-T6 samples (Pergande, 2001), it was found that at micro- level hardness already approached the bulk material property. Thus, a latest hardness test adaptation, namely, nano-indentation, was also used in an effort to observe any potential changes in the material properties at the nano-level.

6.2 Macro-method: Rockwell B Tests

The Rockwell Hardness Tests, along with the Brinell Hardness Tests, is one of the conventional bulk hardness tests that are believed to be non-destructive of the material. Due to the time-consuming nature of the Brinell hardness test along with its general inconsistencies in the hardness data, the Rockwell hardness tests were instead selected to obtain the bulk hardness data. Although the Rockwell hardness tests tend to leave relatively large indentation marks on the surface (up to a millimeter), little surface preparation is required to obtain hardness data, hence quick and efficient. Because the Rockwell B and C tests incorporate different indenter geometries and loads, 1/16 in. diameter steel ball under a 100 kgf major load and a pointed diamond cone under a 150 kgf major load, respectively, both methods were used to compare the results from each other. First, the Rockwell C hardness test, generally used for harder materials, was utilized to obtain the macro-hardness results on all of the cast iron samples at various wear stages. Table 4 records the initial results on the Rockwell C hardness tests from 6 individual measurements, followed by the Rockwell B hardness test from 10 individual measurements recorded in Table 5.

6.2.1 Rockwell C and B Hardness Test Results

From Table 4, it can be seen that all of the Rockwell C measurement results (denoted HRC) are below HRC = 20, which are not within the valid Rockwell C range. The large scatter and inconsistency in the hardness data were due to the fact that this gray cast iron material was too "soft" to be suitable for the Rockwell C test. Therefore, the Rockwell B test was performed to obtain the macro hardness of the gray cast iron samples at various wear stages, and the results are shown in Table 5. Note that the Rockwell B scale is valid up to HRB = 100.

Table 4. Rockwell C Hardness Data

<div align="center">

Rockwell C Hardness Data (HRC)

None Valid (valid only for HRC > 20)

</div>

Measurement	Virgin	¼ x T_{scuff}	½ x T_{scuff}	¾ x T_{scuff}	T_{scuff}
#1	8.9	12.9	7.1	7.3	5.3
#2	8.0	11.0	7.9	9.3	9.0
#3	6.8	9.7	8.9	9.1	11.6
#4	6.3	10.9	7.3	6.3	9.9
#5	6.9	12.9	3.5	9.4	4.5
#6	6.2	8.3	6.5	8.7	4.2
Average	7.2	11.0	6.9	8.4	7.4
Standard deviation	1.1	1.8	1.8	1.3	3.1

Table 5. Rockwell B Hardness Data

	Rockwell B Hardness Data (HRB)					
	All Valid (for HRB < 100)					
Measurement	Virgin		¼ x T_{scuff}	½ x T_{scuff}	¾ x T_{scuff}	T_{scuff}
	Side A	Side B				
#1	94.7	95.7	96.3	93.5	93.5	93.6
#2	95.3	94.0	96.2	94.9	94.4	94.4
#3	95.4	94.0	97.1	93.8	93.6	94.2
#4	93.5	95.2	97.1	95.0	92.5	95.7
#5	95.5	94.6	95.4	93.8	94.1	94.9
#6	95.6	94.8	96.6	94.1	88.6	95.1
#7	96.0	95.1	96.0	93.7	92.5	95.0
#8	95.5	95.3	96.0	92.5	93.0	95.5
#9	94.0	94.5	97.7	93.6	93.1	95.4
#10	94.9	94.0	96.2	94.0	91.9	96.2
Average	95.0	94.7	96.5	93.9	92.7	95.0
Standard deviation	**0.8**	**0.6**	**0.7**	**0.7**	**1.6**	**0.8**

For the virgin sample, the Rockwell B tests were performed on both sides of the specimen (denoted as Side A and Side B) to see if there existed any marked differences in hardness depending on which side of the sample the hardness test was taken from (i.e. "bulk" hardness variation within the sample). From the comparison, both sides of the specimen had a fairly close macro-hardness property. Furthermore, all of the hardness results were below HRB = 100, indicating the validity of the Rockwell B hardness data. Each sample had a relatively small standard deviation between measurements, except in the case of ¾ x T_{scuff} sample, which can be attributed to the significant structural change of the top layer as the surface approaches scuffing.

Figure 37 illustrates a statistical "box and whisker" data (Walpole, 1998). The bottom (blue), middle (red), and top (blue) horizontal lines of each box represent the lower quartile (25 %), median, and upper quartile (75 %), respectively. The whiskers (black vertical lines) extending from top and bottom ends of the box show extreme observations in the sample. The '+' symbols are outlier data, and are only observed for ½ x T_{scuff} case. However, the outlying data at ½ x T_{scuff} should not be taken as the real sample hardness.
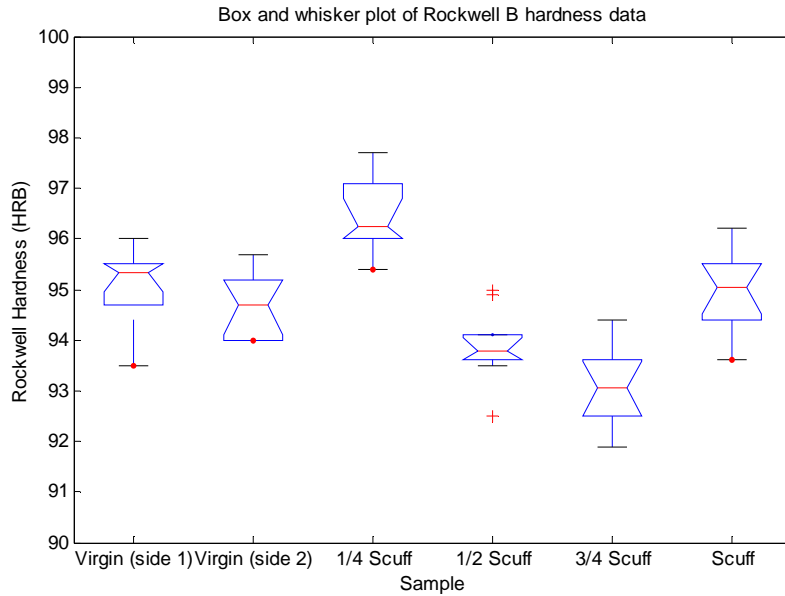
Figure 37. Box and whisker plot of Rockwell B Harndess data

Though hardness at each wear stage appeared to show some differences in Figure 37, the variability was not significant enough to conclude that there were any differences at the macro-level. This was verified in Figure 38, where the same data were plotted for each individual measurement after being converted into standard units, GPa. The Rockwell B hardness (HRB) was converted first to Vickers Hardness (VHN) using a conventional "hardness conversion table", then converted to GPa, following the relation below.

Hardness (GPa) = VHN x 9.8 / 1000

where the factor of 9.8 comes from gravity.
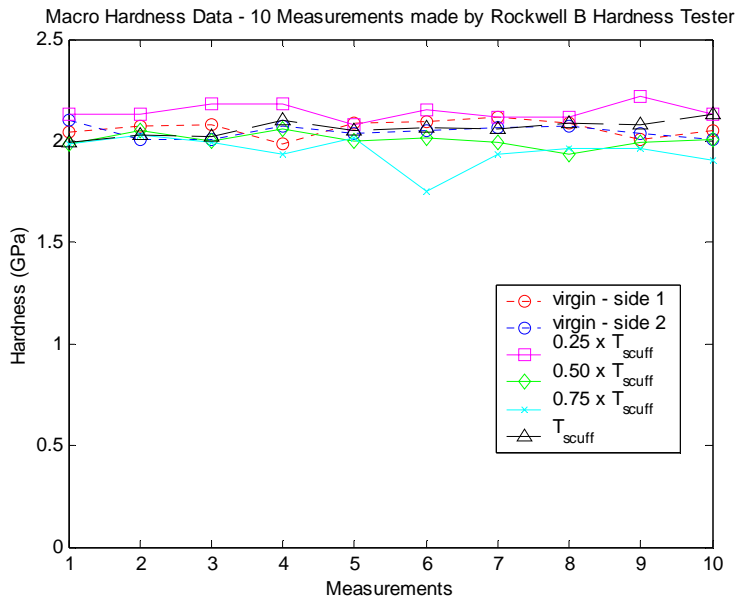
Figure 38. Ten Individual Measurements from Rockwell B Harndess Test

Shown in Figure 38 are significantly overlapping macro-hardness data ranging from 2 to 2.2 GPa, in which no significant wear trend can be observed. By the overall account, the macro-hardness at ¼ x T_{scuff} seemed to be slightly higher than the others, but not large enough to be substantial.

6.2.2 Rockwell B Residual Indents and Residual Depth

Figures 39 (a) through (e) are digital images of residual indents from the Rockwell B Hardness Tests on the gray cast iron material going from virgin to scuffing. From the diameter of residual indentation, the residual depth, or how much the spherical indent has penetrated the surface can be calculated, based on a simple geometric calculations;

$$a = \sqrt{R^2 - \left(\frac{D}{2}\right)^2}$$

$$depth = R - a$$

R = radius of the indenter (1/32 in)

D = diameter of the residual indent (0.73-0.75 mm from Figure 39)

a = distance from the center of the indenter to the surface plane

$depth$ = depth of the residual indentation
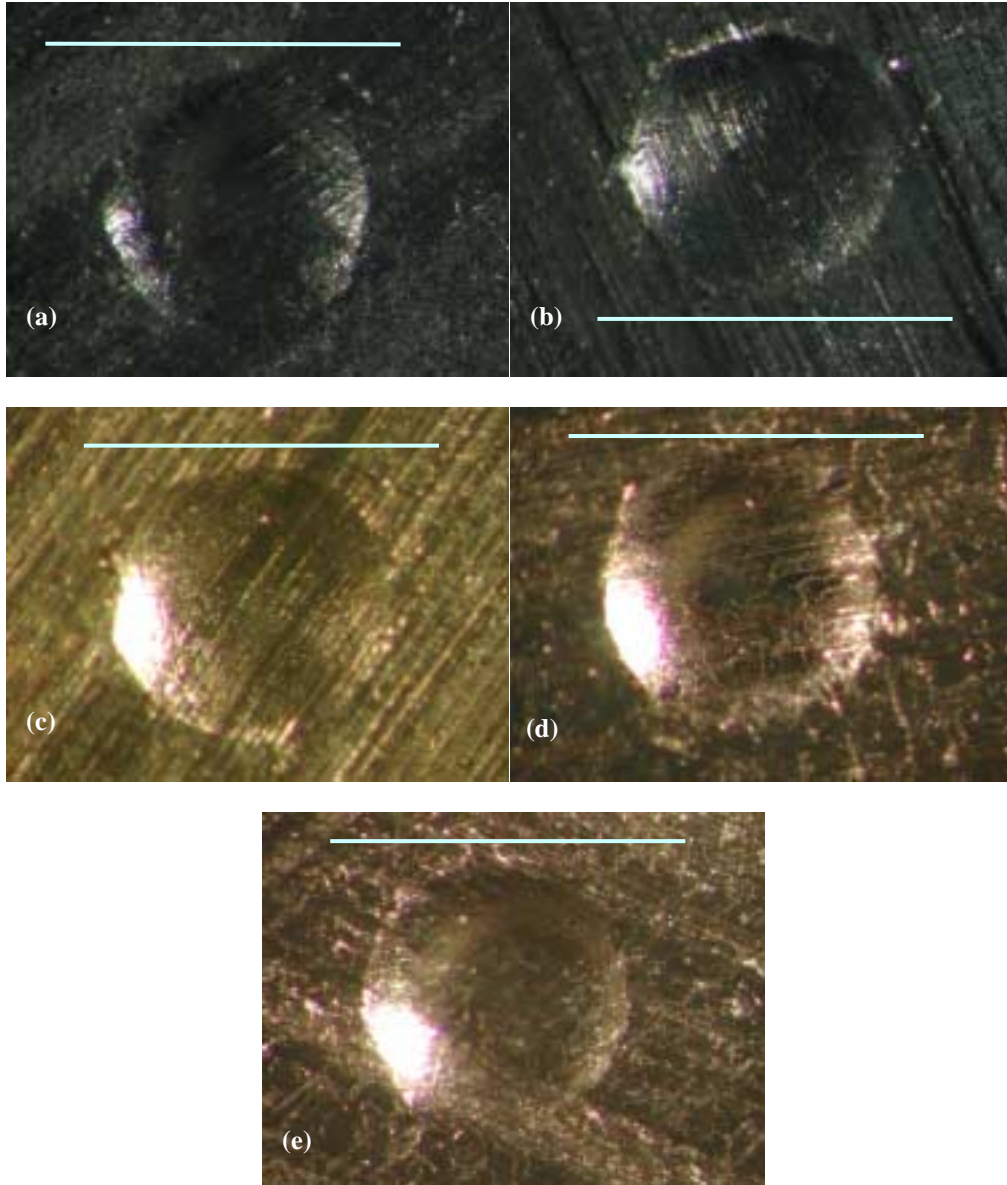
Figure 39. Rockwell B residual indents on gray cast iron (a) virgin, (b) ¼ x T_{scuff}, (c) ½ x T_{scuff}, (d) ¾ x T_{scuff}, and (e) T_{scuff} with horizontal bar marking at 1 mm

From the estimated measurements, the diameter of the residual indent for all of the samples was estimated to be approximately 0.73–0.75 mm long, making the residual depth to be 89-94 µm. Referring to the previous SEM figure of the gray cast iron microstructure (Figure 26), the area affected by a Rockwell B indent seems to be large enough to include a few sparsely distributed graphite particles as well as ferrite-pearlite matrix. This resulted in an averaging effect of the microstructure, proven by the fairly consistent Rockwell B results shown previously.

6.3 Micro-method: Vickers Tests

The Vickers Hardness Test generally measures material hardness for depth range much smaller than those obtained by the Rockwell Hardness Tests. By using the smaller size of the pyramidal shaped indenter with small varying applied loads, the Vickers Tests can give information on changing hardness at micro-scale.

6.3.1 Vickers Hardness Test Results

A Vickers tester uses a diamond Vickers indenter, which is a 4-sided pyramidal with a 136° angle between opposing faces (Pergande, 2001). By defining a certain load available within the tester, which generally ranges from 25 to 500 gf (gram force) or 0.245 to 4.9 N, the indenter tip penetrates the material surface causing plastic deformation to occur. Based on the geometry of the residual deformation measured, defined by the two residual indent diagonals, and the applied load, Vickers Hardness Number (VHN) can be estimated using the relation below;

$$VHN = \frac{1854 \times P}{d_{avg}^{2}}$$

P = load applied to the indenter (gf)

d_{avg} = average of the two residual diagonals measured, d_1 and d_2

$depth = d_{avg}/7$

At first, the surfaces were left "unpolished" since a polishing would alter the wear surface of interest. For each "unpolished" sample, loads of 100, 200, 300, and 500 gf were used, with additional loads of 25 and 50 gf tested for the "unpolished" virgin sample. For samples with wear, lighter loads (i.e. 25, 50 gf) did not generate well-defined plastically deformed indentation marks, and the distorted marks tended to get lost within machining marks, introducing potential errors in hardness statistics while reading the two residual diagonals. Therefore, lighter loads were avoided for the worn samples (Sample 2-5). Furthermore, Vickers indents were repeated twice per worn sample at two different locations of the wear tracks. For Sample 1 (virgin), however, 3-5 tests were performed at different locations for each load. Figures 40 through 41 display the plots of the Vickers hardness data versus (residual) depth for the "unpolished" virgin sample and worn samples, respectively.
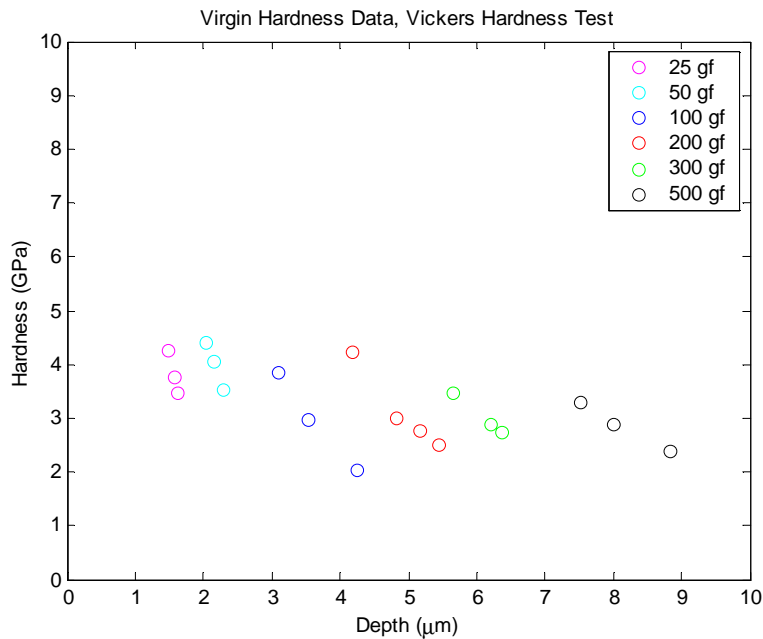

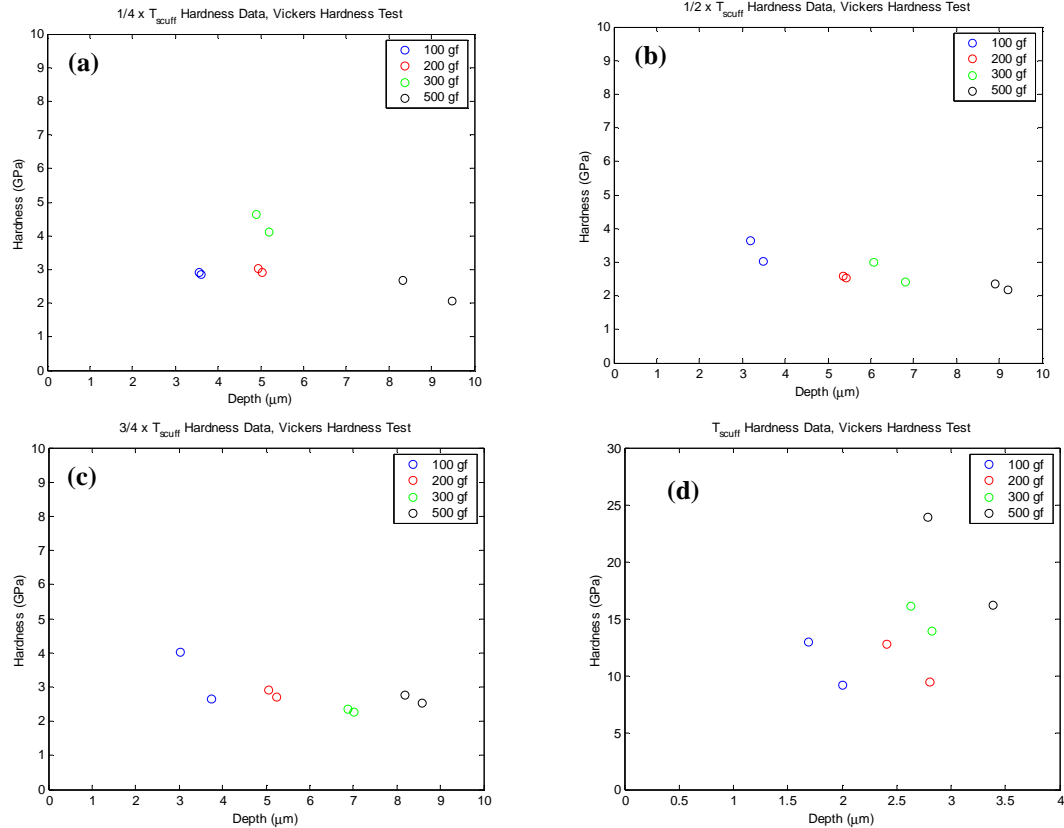Figure 40. Unpolished virgin surface, Vickers Hardness

Figure 41. Worn surface, Vickers Hardness (a) ¼ x T_{scuff}, (b) ½ x T_{scuff}, (c) ¾ x T_{scuff}, and (d) T_{scuff}

Although there appeared to be some scatter in hardness data within each worn sample, the scatter was relatively small to be significant, except in the cases of virgin and T_{scuff} (Figure 41(d)) at which point the surface has essentially failed. The microstructure discussed in Section 4.2 may help explain the fairly consistent hardness results for the worn samples at higher depths. Recall from Figures 26 that the dark graphite flakes are were only randomly dispersed throughout the surface, but also varied in lengths from approximately 30 µm or longer (generally less than 5 µm in thickness). At higher loads (i.e higher depths), the average residual indent diagonals measured approximately from 30 to 60 µm. Therefore, the indent area was large enough to give a combined and averaged hardness effect of graphite and ferrite-pearlite matrix, hence the consistency in the hardness at higher depths.

The scatter or inconsistency of the results in the "unpolished" virgin sample in Figure 40 may be attributed to the influence of surface roughness. Because the surface roughnesses of the virgin gray cast iron samples were relatively high with the R_q of 2-3 µm (compared to the R_q of 1-2 µm or less for the worn samples), the range of peaks and valleys may be up to 8-12 µm. Given a diamond indenter tip of an order of a micron in radius, it then became a matter of where the tip first indented on the surface, in peaks or valleys, or in both. Despite the "averaging" effect of the microstructure, the surface roughness dominated the inconsistency of the Vickers tests for the "unpolished" virgin surface. When the surface was "gently" polished down to the R_q of 0.6 µm with some of its machining marks still visible on the surface, the effects of surface roughness seemed to disappear, resulting in

consistent hardness data, as depicted in Figure 42. With a large sum of peaks and valleys removed from the top surface, the hardness now ranged from 2 to 3 GPa, the most consistent result in all of the Vickers tests performed.
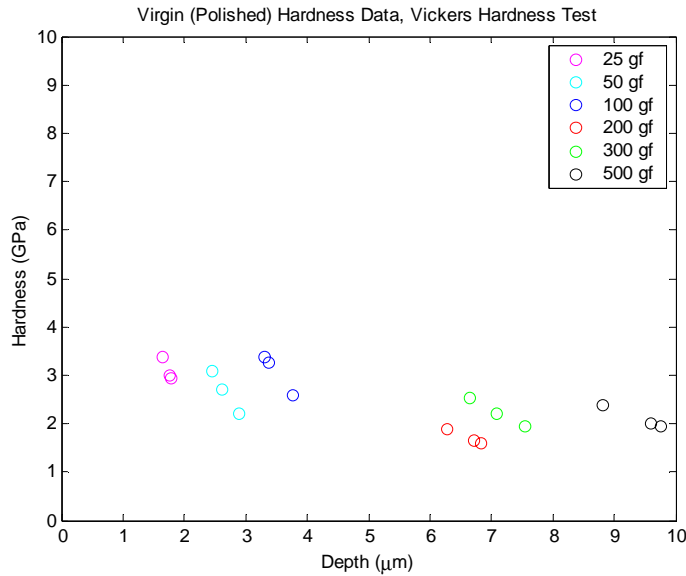
Figure 42. Polished virgin surface, Vickers Hardness

Another important observation made from Figures 40 and 41 was in the slightly increasing global hardness trend for smaller depths, 2 µm or less. This trend became more apparent when all of the Vickers test results were plotted simultaneously as illustrated in Figure 43. Notice from the figure that the spread among the hardness measurements from different samples increased as the depth becomes shallower. When all the hardness data from all wear stages were plotted together, the data points seemed to create grouped trends with varying slopes at several depths, but this was just a coincidental observation and not a real trend (i.e. there were no such trends in individual Vickers hardness plots, Figure 41).
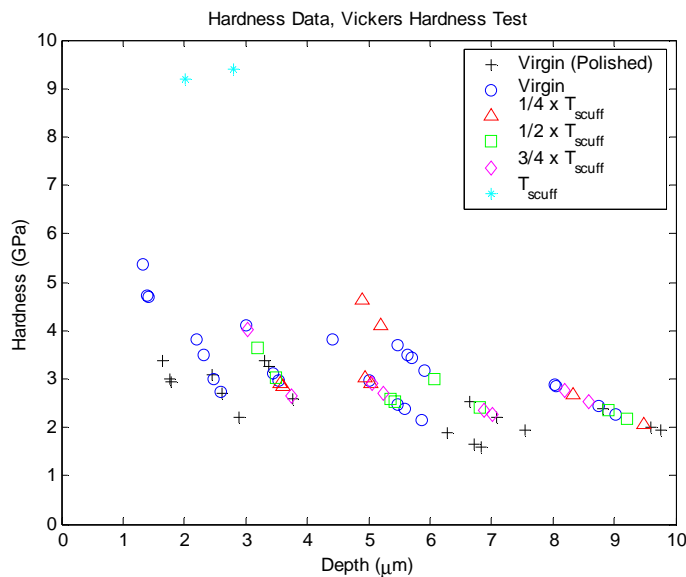
Figure 43. Vickers Hardness values, all samples

The high Vickers hardness values for depths 2 µm or less can be explained by two potential reasons. First, for lower loads such as 25 and 50 gf, average residual indent diagonals measured around 10 µm. At this small load, an indent becomes a highly localized event, most likely indenting an individual microstructural component, namely, either graphite flakes or ferrite-pearlite constituent. In other words, instead of the averaged effect, it now has higher chance to indent graphite alone, which tends to be higher in strength, hence the higher hardness. However, because the "polished" sample shows fairly consistent hardness data irrespective of residual depth, this hypothesis may lack statistical soundness. Next explanation for the higher hardness at shallow depths may be explained by the existence of the lubricant coating, 10-15 % of the top surface. Because the estimated thickness of the coating is 5-10 µm, the Vickers hardness results may be actually those of the coating and not of the cast iron material. For the specified Vickers indentation depths between 1 um and 10 µm, full layers of coating may be present for an "unpolished" virgin sample, while fewer layers or no layer of coating may exist for worn samples. Since the increasing trend at shallow depths is most evident in the "unpolished" virgin sample, this seemed a valid explanation for the observed behavior of increasing hardness. Figure 42 further supported the theory of the lubricant coating. For the polished sample, more than 10 µm of top surface layer was removed from the surface roughness ($R_{p\text{-}v}$ for unpolished virgin ≈ 8-12 µm to $R_{p\text{-}v}$ for polished virgin ≈ 2.4 µm). This ensured the removal of the coating layer in the polished sample, hence the consistent hardness results.

6.4 Nano-method: Nano-indentation

From the seemingly increasing trend in hardness observed in the Vickers tests for shallow depths, 2 µm or less, the investigation of the mechanical properties was continued at the nano-scale in this section. The current existing hardness techniques at the nano-scale include nano-indentation and nano-scratch. Both techniques are based on macro/micro hardness test principles where material hardness is extrapolated from a material resistance to permanent plastic deformation. While nano-indentation technique involves pressing an extremely sharp, diamond tip into a surface, nano-scratch technique uses a even sharper (i.e. higher aspect ratio) conical diamond tip to traverse along a surface at a user-prescribed vertical load. Though the latter technique avoids acquiring localized effects thereby producing a more uniform, "averaged" result, it is more time-consuming and intricate to produce a result. Furthermore, the final hardness data acquired by nano-scratch are not quantitative, but qualitative in nature (i.e. hardness in GPa vs. average scratch depth). For more on nano-scratch, refer to Pergande (2001). Although nano-indentation technique has yet to overcome some of its major drawbacks in interpretation of its data largely statistical in nature, nano-indentation was used since it yields quantitative hardness data along with quantitative elastic modulii. Also by using different indenters with varying tip radii and aspect ratios, i.e. Berkovich tip and 90° cube corner tip, nano-indentation method can yield hardness information from 200 nm down to less than 50 nm deep from the top surface.

The nano-indentation instrument used is a Triboscope Nano-Indenter made by Hysitron, Inc. The Triboscope is attached to a Scanning Probe Microscope (SPM), which enables in-situ scanning of the indenting surface, much like a conventional Atomic Force Microscope (AFM). Refer to the Hystrion website (http://www.Hysitron.com) for detailed instrument specifications.

6.4.1 Nano-indentation Background

Areas where the nano-indentation technique is used most successfully are the semi-conductor and magnetic storage Hard Disk Drive (HDD) industries, in which extremely thin films exist and their material properties may be of special interest. Surfaces studied in such applications are extremely smooth and relatively uniform, thereby making nano-indentation acquired hardness results optimal and reliable. In the case of studying the uppermost 200 nm layer of a "rough" engineering surface such as gray cast iron, it was initially anticipated that the nano-indentation hardness results may not be entirely consistent or accurate. Due to the nature of the non-uniform microstructure of gray cast iron composed of graphite and ferrite-pearlite matrix, the hardness data may still be of highly localized effects. However, since the gray cast iron does not have grains or grain boundaries, the degree of localization may be less severe than in the case of Al390-T6 samples for instance (Pergande, 2001). This was the premise of adopting the nano-indentation technique in this section.

Because the material surface was considerably rough, we avoided using a cube-corner tip not only because the tip may be damaged during the process of indentation but also that it may not produce statistically sound results. Instead, the Hysitron Berkovich tip was used for all of the cast iron samples for the analysis of penetration depths down to 200 nm. The Berkovich tip had been initially calibrated for *contact* depths between 53 nm and 187 nm, outside which hardness data were considered invalid.

For the choice of loading/unloading function, pull-load (multiple load-unload functions were sequentially applied at the same indentation site) rather than a ramp-load for single indents is chosen, varying at the final maximum load and total loading time. It has been reported that pull-load indeed provides consistent and accurate results despite multiple indents made at the same location (Pergande, 2001). Because each successive load segment has higher load than the previous load curve, strain hardening does not play a role in pull-loading. Pull-load is advantageous since it can achieve several hardness data points at one setting without having to move to different indentation sites each time, thereby increasing its data acquisition efficiency. The range of maximum pull-loads used in this experiment was from 1000 µN to 5000 µN. Note that in order to ensure the accuracy of instrument operation, nano-indentation is always performed on a standard material (i.e. fused quartz) to calibrate the instrument before running any tests on the cast iron samples.

6.4.2 Nano-indentation Results

As stated earlier, nano-indentation tends to produced localized hardness values, generating considerably scattered hardness values. This is mainly due to the existing engaging mechanism of the SPM system, which leaves little room for controlling the sites of indentation. When combined with the small radius of the Berkovich tip ranging between 100-200 nm, it becomes quite difficult a task to ensure indentations to be limited to asperities rather than peaks or valleys, in order that the measurement errors are best minimized. Figures 44(a) and (b) show the loading curves obtained with pull-load functions at various maximum loads, for the unpolished virgin and ¾ x T_{scuff} samples, respectively.
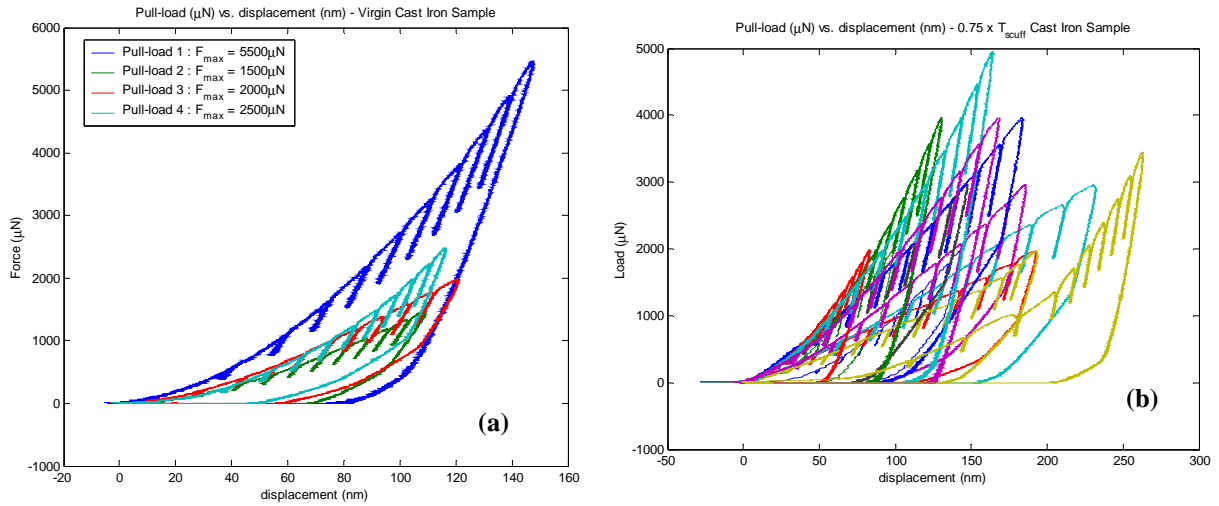
Figure 44. Loading curves (pull-loads) obtained by the Berkovich tip; (a) unpolished virgin, (b) unpolished ¾ x T_{scuff} gray cast iron samples

If a material is highly non-uniform with the presence of various naturally occuring oxide layers, the loading curve slopes within a sample generally differ quite significantly. This was indeed the case for all five of the unpolished cast iron samples at various worn tribological stages. As the surface was more worn as it evolved toward scuffing, the slopes of the loading curves were not only different from one another, but the maximum contact depths varied significantly from one another as well. Shown in Figure 45 is the associated hardness and reduced elastic modulus for the unpolished virgin sample, or translated material properties with the great amount of scatter in the sample, hence the material data are of no trustworthy source.
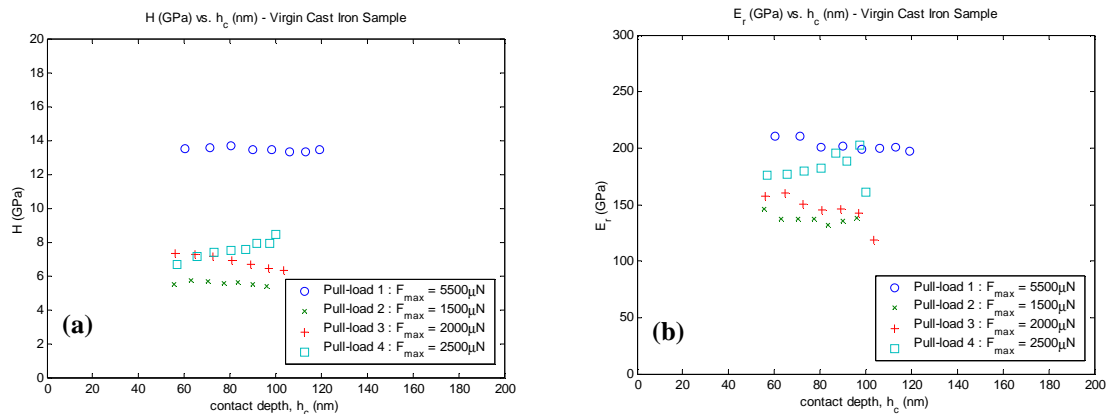

Figure 45. Unpolished virgin sample (a) hardness and (b) reduced elastic modulus data

Recall that the hardness and elastic modulus results were only valid for contact depths specified for 53-187 nm using the Berkovich indenter. The amount of scatter in the hardness and elastic modulus data ranged from 5 GPa to 13 GPa and from 150 GPa to 200 GPa, respectively; these data ranges were too large to be considered neither "real" nor accurate. Similarly, all of the worn samples showed a large amount of scatter in their respective data, typically ranging from 2 GPa to 12 GPa in hardness and from 50 GPa to 300 GPa in elastic modulus.

The main reason for such high discrepancy within a sample was localized, non-uniform surface roughness. From the previous Vickers tests, it has been demonstrated that the scatter in hardness data can be minimized when the surface is polished. To make certain it holds true, even at the nano-level, that the scatter within each sample was due to surface roughness and not microstructure, the polished virgin specimen used in the previous Vickers test was reused for nano-indentation. Figure 46 shows the SPM (Scanning Probe Microscope) captured images of two different engaging sites on the polished sample. The apparent scratches on the images were from the machining marks that were not completely removed from the "gentle" polishing. Although an earlier Dektak profilometer measurement showed that R_q of the polished cast iron sample was approximately 0.6 µm over a 4 mm scan, the R_q became 2 orders of magnitude smaller when the area computed for surface roughness was limited to a much smaller size (i.e. 4 µm by 4 µm).
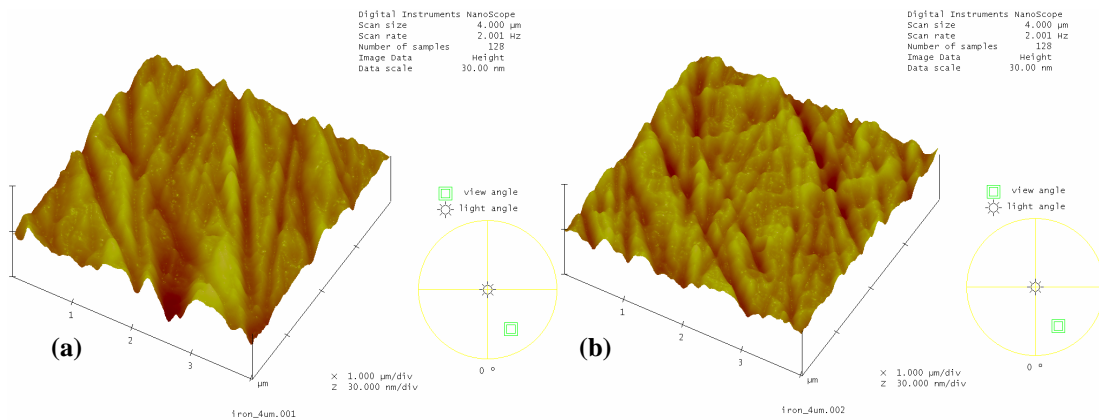
Figure 46. SPM images of polished virgin cast iron sample at two different locations (a) R_q = 3.4 nm, (b) R_q = 2.4 nm

The pull-load loading curve for the polished sample was plotted in Figure 47, whereas the associated hardness and elastic modulus data were plotted in Figures 48 and 49, respectively.
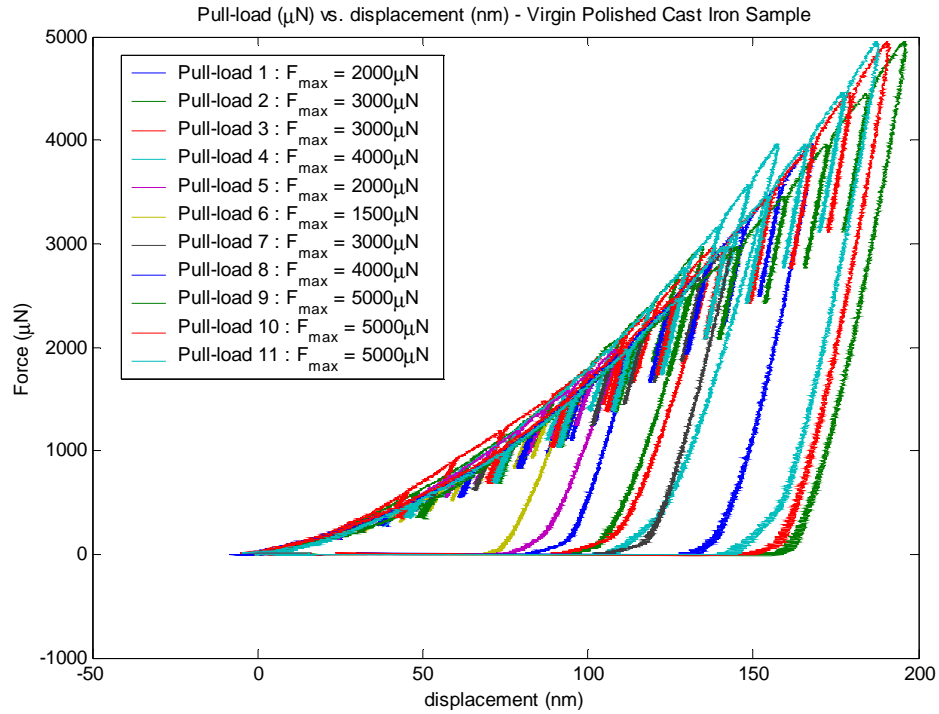
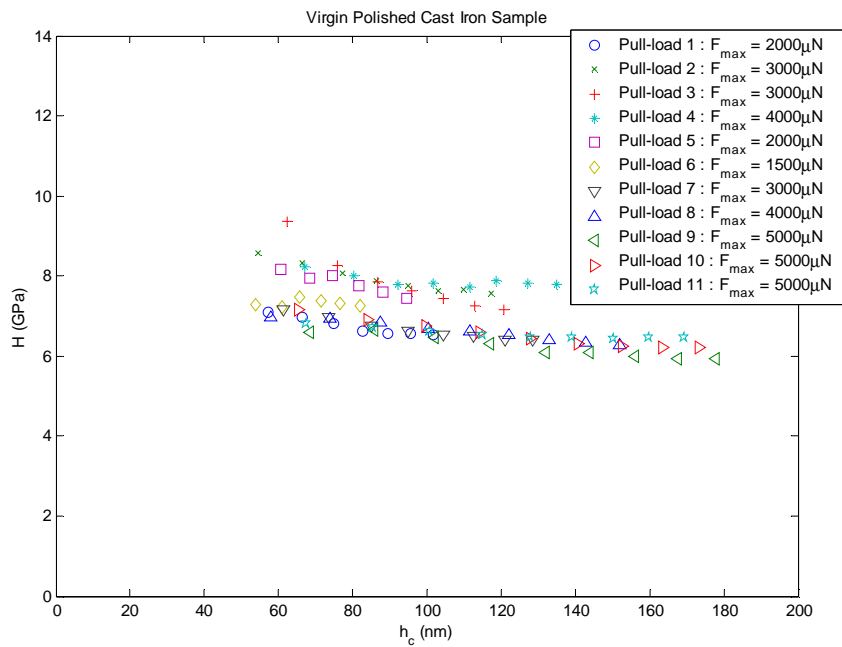Figure 47. Polished virgin sample loading curve obtained by the Berkovich tip

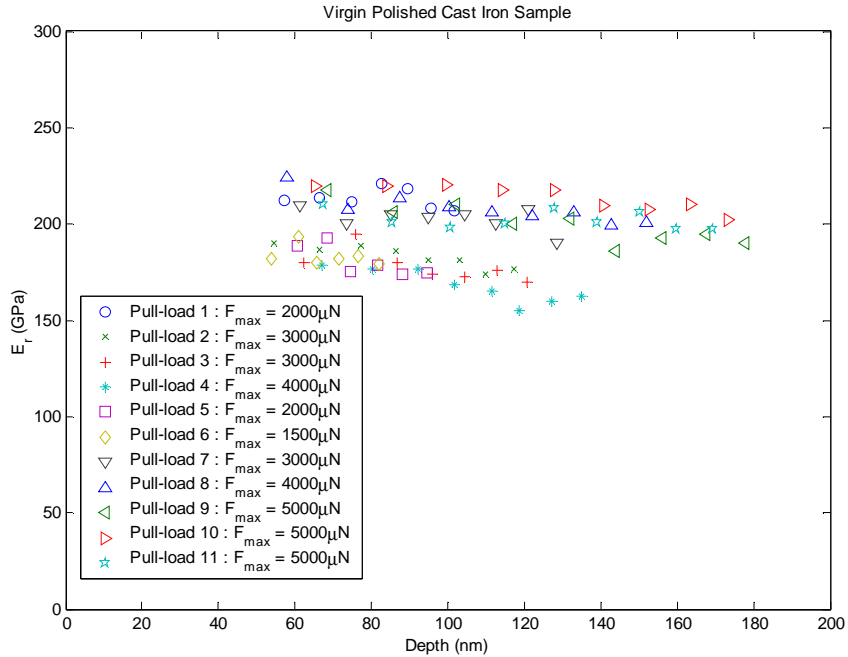Figure 48. Polished virgin sample hardness data

47

Figure 49. Polished virgin sample reduced elastic modulus data

Once the dominant surface roughness features such as peaks and valleys were removed from the polishing, nano-indentation results were fairly consistent and uniform. Although there was some amount of scatter in hardness and elastic modulus data, it was relatively insignificant compare to those of the untreated, unpolished virgin and worn samples. The little amount of scatter could be attributed to the "small", location-dependent surface roughness that was not removed by the "gentle" polishing process (guided by visual judgment). From the relatively uniform hardness and modulus data despite the high localization, it was concluded that the different microstructural constituents, graphite and ferrite-pearlite, may possess similar material properties. The uniform slopes displayed by the loading curves in Figure 47 suggested that a criteria curve, by which one can differentiate different material components was not needed, and further supports the theory of similar hardness properties among the microstructures.

6.5 Conclusion on Macro-, Micro-, and Nano- Hardness

Several existing "indentation" methods, both conventional macro/micro techniques and current nano technique, have been used to investigate the material properties of the uppermost layers of gray cast iron as the surface goes through tribological wear. In order to investigate any significant trends in hardness at all scales, the macro-scale data from Rockwell B tests, micro-scale data from Vickers indents, and nano-scale data from nano-indentation experiments were combined on a single plot, as appeared in Figure 50. From this figure, hardness data from various depths were displayed covering a range of over four orders of magnitude (200 nm – 10 µm). The most noticeable trend was that the top 200 nm shows a significant higher hardness than the rest of the data. The hardness at a depth of 50-200 nm was 6-8 GPa, which decreased to 2-4 GPa at a depth of 1-10 µm. The higher hardness at the nano-level depths may be due to the formation of protective oxide layers. Since this virgin sample has been

polished, the protective lubricant coating was mostly removed, thus may not contribute to the hardness at this region.

One difficulty in making a sound conclusion on overall hardness analysis was the missing data region approximately between 200 nm and 1 μm depths. Because there was no equipment available at the given facility that would obtain intermediate hardness variation between the nano- and micro- levels, an intelligent conjecture connecting the two scales must be made for this region. Once the conjecture was made, in Figure 50, the hardness data from nano-indentation seemed to continue to decrease to about 10 μm, from which hardness was seemingly reached a steady bulk property picked up by the Rockwell B test. This behavior was not observed in the previous hardness analysis of Al390-T6 alloy samples (Pergande, 2001), where the hardness already reached a steady bulk property from the depth of 1 μm, the starting depth range covered by the Vickers tests.
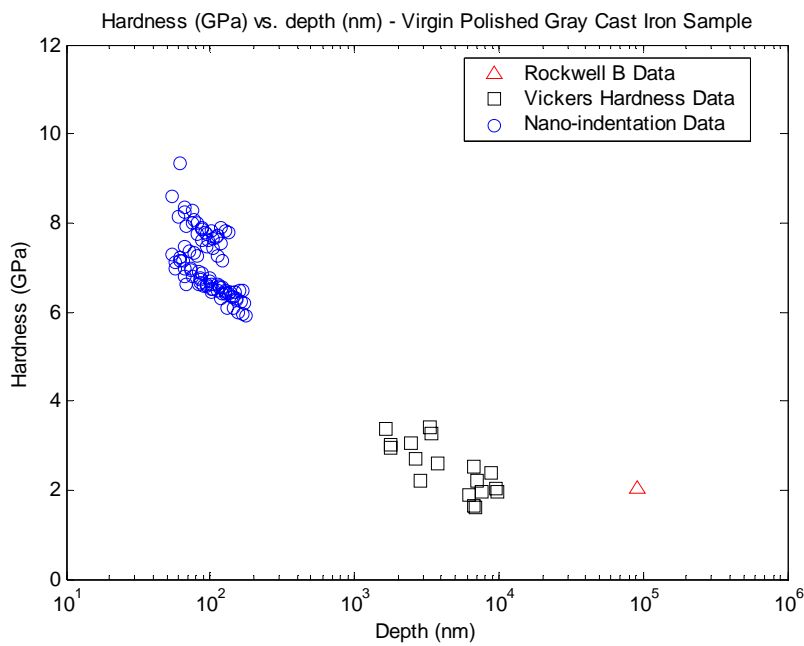

Figure 50. Polished virgin gray cast iron sample hardness continuum

Chapter 7. Conclusion

In many engineering applications, surfaces in prolonged contact may experience abrupt catastrophic failure in the form of scuffing. In order to prevent such failure, not only is one required to observe and investigate the physical changes that happen in the material during wear and damage, but also gain insights in how damage mechanisms progress in relation to given environments, in hopes to minimize and eliminate scuffing. Because most crucial damage occurs at the uppermost surface layer of engineering surfaces, various types of analyses have been conducted at the subsurface-level. The changes occurring on the uppermost surface layer accompanied by the onset of scuffing include changes on topographical, micro-structural, chemical, and material properties. As each chapter of this report was dedicated to discussing different techniques to characterize these changes, no single analysis was found to be a stand-alone process by which scuffing mechanism was comprehensively understood. Surface roughness characterization of the worn disks and pins revealed some aspects of geometric evolution of the surface topography, but no distinct behavior by which scuffing was signaled could be noted. The top-surface microstructure analyzed by the SEM was helpful in observing the essential 'bulk' surface microstructural constituents of gray cast iron, but only upon polishing and etching of the sample. The SEM method that would have reserved much of the original surface and subsurface features was the cross-sectional SEM profile. At a sufficiently high magnification, cross-sectional SEM images may have shown evidence of possible thermal and mechanical changes occurred on the material at the nano through micro- scales. Despite the lack of clear trends, the AES chemical analysis was found to be the best method in which the effects of scuffing was unmistakably signaled by the drastic changes in its chemical element composition. The AES analysis was also a more practical engineering approach compared to that of the latest material property extracting methods such as nano-indentation technique. Material hardness data for a polished virgin cast iron samples at the macro-, micro-, and nano- levels have been individually acquired through the existing indentation methods. Although there was some decreasing trend in hardness with increasing contact depth, the mechanism causing this behavior was not well understood.

References

Callister, W.D., 1997, Materials Science and Engineering: An Introduction, John Wiley & Sons, Inc., 4th ed.

Cavatorta, M. P., and Cusano, C., "Running-in of aluminum/steel contacts under starved lubrication Part II: Effects on scuffing," *Wear,* 242 (2000), pp. 133-139.

Greenwood, J. A., and Williamson, B. P., 1966, "Contact of Nominally Flat Surfaces," *Proc. R. Soc. London, Ser A,* **295**, pp. 300-319.

McCool, J.I., 1986, "Comparison of Models for the Contact of Rough Surfaces," *Wear*, **107**, pp. 37-60.

Patel, J.J., 2001, Investigation of the Scuffing Mechanism Under Starved Lubrication Conditions Using Macro, Meso, Micro, and Nano Analytical Techniques, M.S. Thesis, University of Illinois at Urbana-Champaign.

Pergande, S.R., 2001, Use of Nano-Indentation and Nano-Scratch Techniques to Investigate Near Surface Material Properties Associated with Scuffing of Engineering Surface, M.S. Thesis, University of Illinois at Urbana-Champaign.

Shackelford, J.F., 1988, Introduction to Materials Science for Engineers, Macmillan Publishing Co., New York, NY, 2nd ed.

Stout, K.J., Sullivan, P.J., Dong, W.P., Mainsah, E., Luo, N., Mathia, T., Zahouani, H., 1993, The Development of Methods for the Characterization of Roughness in Three Dimensions, Commission of the European Communities, Brussels-Luxembourg.

Vander Voort, G., 1999, "Preparation of Cast Aluminum-Silicon Alloys," *Tech – Notes: Using Microstructural Analysis to Solve Practical Problems*, Buehler Inc., Volume **3**, Issue **2**.

Walpole, R. E., Myers, R. H., Myers, S. L., 1998, Probability and Statistics for Engineers and Scientists, Prentice Hall, New Jersey, 6th ed.

Yoon, H. K., 1999, Scuffing Under Starved Lubrication Conditions, PhD Thesis, University of Illinois at Urbana-Champaign.